Crystal plasticity modeling of microstructure influence on fatigue crack initiation in extruded Al6082-T6 with surface irregularities

Håkan Hallberg †*, Sigmund Kyrre Ås ‡, Bjørn Skallerud ‡
† Division of Solid Mechanics, Lund University, P.O. Box 118, SE-221 00 Lund, Sweden
‡ Norwegian University of Science and Technology
Department of Structural Engineering, 7491 Trondheim, Norway

Abstract

The influence of surface roughness and microstructure heterogeneities in the vicinity of macroscopic stress concentrations are investigated by crystal plasticity simulations. It is shown that in the extruded Al6082-T6 alloy under consideration, twin grain boundaries and other highly misoriented grain interfaces, which constitute significant barriers to plastic slip, provide internal domains in the material where initiation of fatigue damage is more likely to occur than at the stress concentrations which are due to the surface roughness. In addition, the microstructure influence on the appearance of stress gradients is found to be significant. Further, the present study indicates that frequently used fatigue initiation parameters (FIP) such as the locally accumulated plastic strain or stored energy may be insufficient to identify fatigue crack initiation. Such parameters should be complemented or replaced by other FIP which take additional characteristics of the microstructure into account. This is exemplified in the present study by employing two additional FIPs, based on a modified Fatemi-Socie critical-plane parameter and on the Dang Van criterion, respectively.

Keywords: Fatigue crack initiation, Crystal plasticity simulations, Aluminum, Stress concentrations, Texture

1 Introduction

Classically, fatigue crack initiation is analyzed by identifying regions in components with macroscopic stress concentrations, and the component's fatigue life is usually assessed based on macroscopic data such as stress- or strain-life curves and Goodman diagrams. Much effort has been put on fatigue testing of specimens with surfaces polished to a mirror-like finish in order to establish well-defined fatigue strength parameters and to identify the fundamental mechanisms involved in fatigue crack initiation. Part of this work has been directed at

*Corresponding author. Mail: hakan.hallberg@solid.lth.se. Tel.: +46 46 222 90 92.

quantifying the extrusion-intrusion mechanism, causing surface roughening during fatigue. While such test results are indispensable for metallurgists, they are often difficult to apply in engineering design since some degree of surface roughness cannot be avoided. The classical approach is to employ empirical correction factors to account for surface irregularities, see for example [24]. Today, the experimental toolbox has grown to also include, for example, non-contact high resolution scanning methods (typically using lasers or white light interferometry). Such methods permit detailed mapping of surface topographies. How to use such information in fatigue life assessments is, however, still an open question. Mapping of surface roughness and relating it to fatigue damage initiation is addressed in [1, 2] and the findings in these studies serve as a starting point for the present work.

In addition to geometric parameters such as macroscopic notches and surface roughness, also microstructural properties play a central role in determining a components susceptibility to fatigue crack initiation and subsequent failure. A component's surface roughness usually correspond to microscopic surface notches, typically of the same scale as the grain size or other characteristic dimensions in the microstructure. As noted in for example [31], fatigue damage initiates and evolves due to a vast range of microstructure mechanisms and features. These include, for example, debonding between inclusions and the matrix material, interaction between slip bands and grain boundaries, fracture along grain boundaries and presence of surface irregularities. The importance of local slip irreversibility and slip interaction with other local microstructure heterogeneities is thoroughly discussed in [40].

The influence of the microstructure properties on fatigue crack initiation and propagation has been approached by numerical simulations across length scales, ranging from discrete dislocation dynamics modeling [12] to continuum mechanical formulations [45]. In particular, a number of studies exist in which crystal plasticity simulations are used as a tool to investigate how fatigue crack initiation and propagation is affected by the microstructure. Such an approach is, for example, used in [51] to study the fatigue life of a superalloy at high temperature and to investigate fatigue crack initiation in an Al7075 alloy in [28]. Factors as crystallographic texture and grain size are observed to influence fatigue crack initiation. In [46], crystal plasticity simulations and four-point bending experiments indicate that the location of fatigue failure coincide with the highest concentrations of geometrically necessary dislocations. High-cycle fatigue properties of a ferritic-pearlitic steel are simulated using crystal plasticity in [18]. Modeling of fatigue crack growth in a Ni-based superalloy and the influence of grain boundaries is discussed in [36]. A comprehensive overview of microstructure-sensitive fatigue modeling is provided in [31].

In the present work, crystal plasticity modeling is used to investigate the role of the microstructure on the local conditions for fatigue crack initiation in an extruded aluminum alloy Al6082-T6. The study is a continuation of the work in [1] where it was noted that fatigue cracks in bars of Al6082-T6, loaded under cyclic tension/compression, are generally initiated at surface topography irregularities which do not coincide with the locations holding the highest stress concentrations. Elastic-plastic finite element analyses were also used in

[1] to show that the stress field in the notch region play an important role, in accordance with the classical works by Neuber [38] and Sibel and Stieler [44]. Use of such classical approaches did, however, turn out to be inconclusive with regard to fatigue life prediction of rough surfaces [1, 3]. These approaches are based on the assumption that the fatigue limit condition is governed by the stress field some distance ahead of the notch. A lower gradient means that the notch field reaches further into the material and may engage more grains and grain boundaries, which thereby contribute to the initiation of fatigue cracks. Furthermore, the closed-form solutions for notch sensitivity assume that the notch is symmetrical and not influenced by nearby notches. This is not necessarily the case for notches that make up a rough surface.

More recent adaptations of these classical theories for notch fatigue problems make use of linear elastic finite element analysis [47], where notches may have arbitrary shapes and configurations. In [1], it is shown that the fatigue limit condition due to surface roughness can be determined based on the stress range a certain "critical" distance away from the notch tip, or by averaging over a certain length.

The application of these theories in the finite-life region is more challenging since the stress field at the critical distance may be influenced by plasticity. The notches are on the same scale as the grain size, and thus the assumption of a homogeneous material is not strictly valid. The present study elaborates on the previous work in [1, 2] by also considering the influence of microstructure heterogeneities such as grain boundaries and grain misorientation in the vicinity of surface irregularities.

A consistent trend in the previous studies [1, 2] is that fatigue do not occur in notches with the highest stress concentration factors, but rather in blunt notches with low stress gradients. The aim of the present work is to investigate whether variations in grain size, grain boundary configurations and crystallographic orientations can explain this behavior. A number of established fatigue initiation parameters are considered for identification of likely fatigue crack initiation sites in the material.

In the present paper, Section 2 summarizes the central features of the previous experimental investigations presented in [1, 2], which provide the background and experimental input to the present study. The adopted crystal plasticity formulation, the simulation model and the chosen set of fatigue initiation parameters is discussed in Section 3. The results from the numerical simulations and a discussion on the findings follow in Section 4 and some concluding remarks close the paper in Section 5.

2 Experiments

As part of previous research on fatigue life prediction for an Al6082-T6 aluminum alloy automotive component, presented in [1], a significant body of data on fatigue crack initiation in this material was generated. A large number of cylindrical bars made of extruded Al6082-T6 were subjected to constant amplitude cyclic tensile/compressive loading until fa-

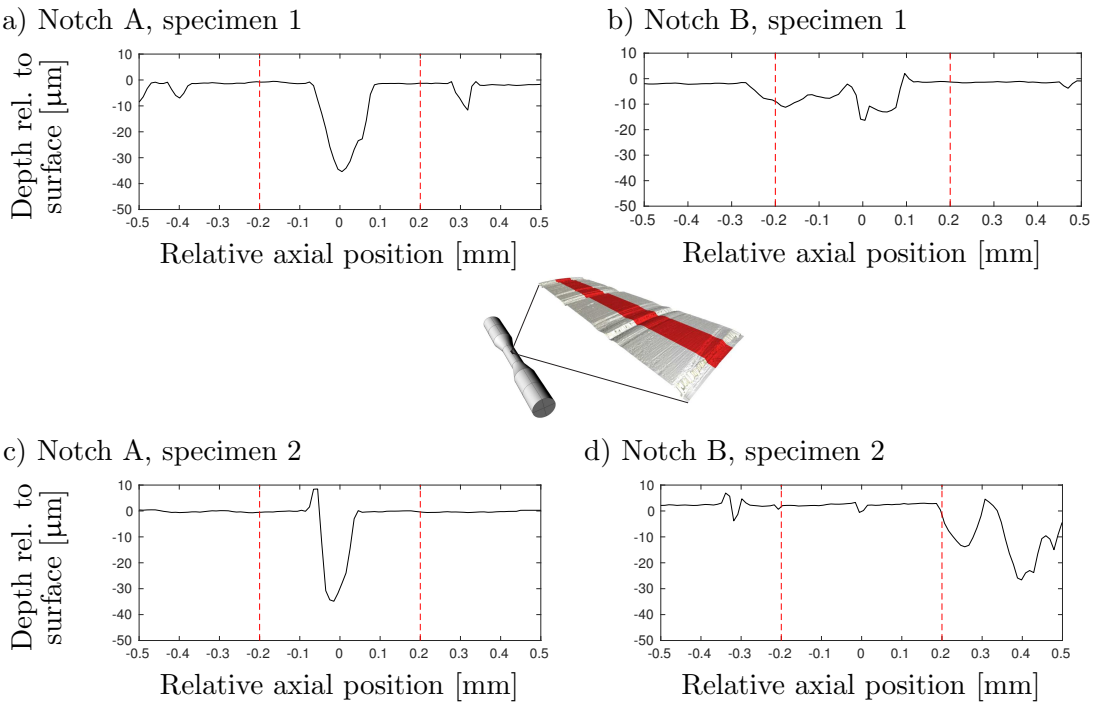

Figure 1: Surface profile mappings acquired by White Light Interferometry (WLI) in [1]. Figures a and b show surface regions along the same test specimen, here denoted "Specimen 1", and figures c and d show surface regions along another test specimen, here denoted "Specimen 2". Fracture was in both specimens initiated at Notch A although a considerably higher stress concentration was found at Notch B. The dashed red lines correspond to the limits of the regions which are used in the crystal plasticity simulations in the present work. The picture inlay illustrates a WLI scan along one of the test specimens, taken from [1].

tigue failure. Surface roughness was introduced on the cylindrical specimens in a way that permitted axisymmetric modeling of the topography. The roughness severity was varied with $R_a = \frac{1}{L}\int_L |z| dL = [2.2 - 11]$ µm and deepest valleys in the range of 10-40 µm. The geometry and stress concentrations at notches along the specimens were carefully examined prior to the experiments and matched against the fatigue failure sites *post mortem*. The surface topography was mapped using a Wyko NT2000 white light interferometry (WLI) profilometer and the WLI measurements were used to provide 2D surface roughness profiles. After fatigue testing, it was possible to identify the notch that governed the fatigue crack initiation with the aid of a stereo microscope. The surface profiles were used to generate axi-symmetric finite element models of the specimens, using both linear elastic and elastic-plastic constitutive models to evaluate the stress concentrations at the surface irregularities. This methodology is detailed in [2]. It was found that in the majority of cases fatigue failure did not initiate at the notch with the most severe stress concentration.

As representative cases, taken from the studies in [1, 2], Fig. 1 shows surface profile mappings of two different test specimens. The dashed red lines in Fig. 1 show the limits of

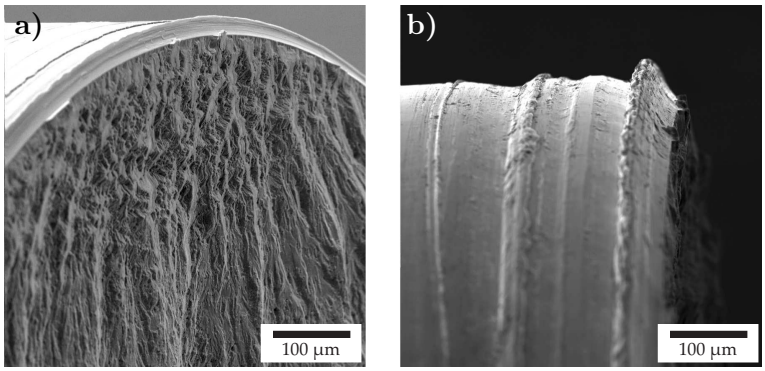

Figure 2: SEM images of a typical fracture surface, oriented orthogonal to the loading direction in the extruded material, taken from [1]. The fatigue fracture has originated at the bottom of one of the surface grooves.

the surface profiles employed in the crystal plasticity simulations performed in the present work. The notches shown in Figs. 1a and b are from one specimen ("Specimen 1") and the notches in Fig. 1c and d are from another specimen ("Specimen 2"). In both cases, fatigue failure was initiated at "Notch A", although a considerably higher stress concentration was found, by the elastic-plastic finite element simulations performed in [1], at "Notch B". Some characteristic fracture surfaces are illustrated in Fig. 2. The notches denoted by "Notch B" in specimens 1 and 2 are representative for a number of surface irregularities which provided higher stress concentrations than those found at the actual To further illustrate this trend, Fig. 3 shows axial stress values beneath the deepest point of all major notches that were investigated in specimens 1 and 2. The results were obtained from nonlinear elastic-plastic finite element analysis, using a bi-linear kinematic hardening model and the cyclic stress-strain curve, as discussed in [1]. In Fig. 3 the axial stress is normalized by the cyclic yield stress of the material. The red lines in Fig. 3 correspond to Notch A in each specimen and the blue lines correspond to the stress variation beneath Notch B.

The specimens with the notches shown in Fig. 1 were tested with a stress ratio of $R = -1$, i.e. with zero mean stress. The specimen in Fig. 1a-b was tested with a stress range of 370 MPa and the specimen in Fig. 1c-d with a stress range of 300 MPa. These stress ranges correspond to strain amplitudes of approximately 0.25 % and 0.20 %, respectively. The specimens were tested until fatigue failure, which occurred after 121 315 cycles for the specimen subjected to the higher stress amplitude (Specimen 1) and after 395 633 cycles for the specimen subjected to the lower stress amplitude (Specimen 2). The cyclic loading is further discussed in relation to calibration of the crystal plasticity model in Section 3.2.

Additional microstructure characterization was performed as part of the work in [1]. Fig. 4 shows an EBSD mapping of the microstructure, which is representative for the material. It can be noted that the microstructure is dominated by grains which are significantly elongated along the extrusion direction (ED). As discussed in the introduction, the presence and char-

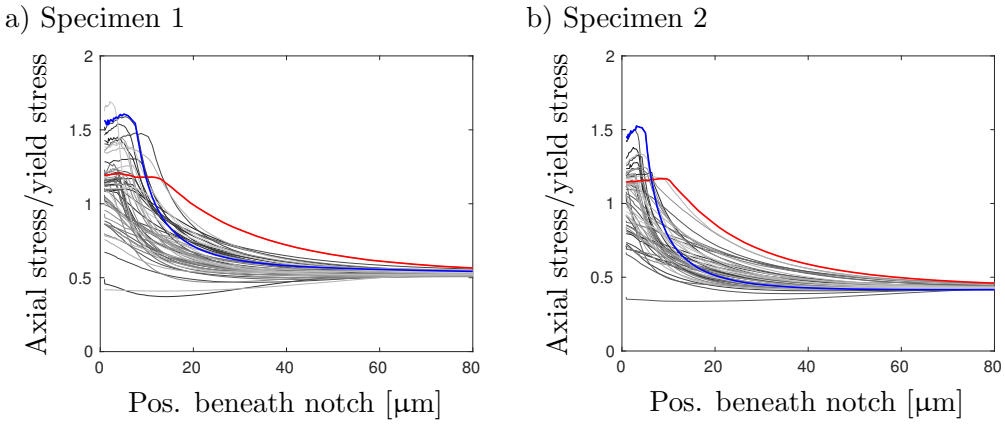

Figure 3: Stress variations beneath all major notches in specimens 1 and 2 examined in [1]. The vertical axes show the axial stress, as evaluated by nonlinear elastic-plastic finite element analyses and normalized by the cyclic yield stress. The red lines correspond to Notch A (initiation notch) and the blue lines correspond to Notch B in each specimen. The notch geometries are shown in Fig. 1.

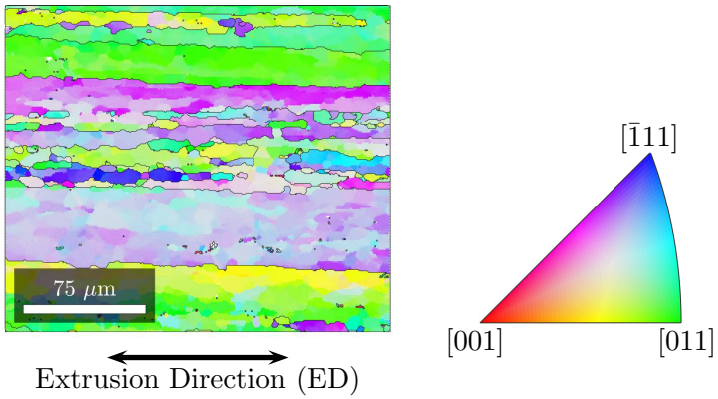

Figure 4: EBSD map of the cross-section of the extruded material. The grains are elongated along the extrusion direction (ED). The loading direction is in the same direction.

acter of grain boundaries have a major impact on fatigue crack initiation. A key factor is the presence of high-angle grain boundaries which constitute significant barriers to plastic slip in the material [6, 33]. Such restricted slip may cause accumulation of dislocations at grain boundaries and serve as an initiation mechanism for fatigue damage [40]. Special attention is therefore paid presently to the grain boundary structure in the extruded material under consideration. Fig. 5a shows a grain boundary map where the EBSD data has been used to calculate the misorientation along the grain boundaries. It can be noted that the grain boundary network is dominated by high-angle grain boundaries. Fig. 5b shows the same grain boundary map, but with the boundaries color-coded according to their Coincidence Site Lattice (CSL) correspondence. It is seen that part of the grain boundary network constitute $\Sigma 3$ twin boundaries. The formation of twin boundaries is usually associated with materials of low stacking-fault energy, such as Cu and Ag, and not materials with higher stacking-fault energy such as Al. But the prior extrusion process has in the present case led to deformation-induced twinning in the material.

Pole figures, corresponding to the EBSD data in Fig. 4, are shown in Fig. 6 and reveal a characteristic extrusion texture in the material. The red markings in Fig. 6 correspond to the subset of 500 representative crystal orientations used in the calibration of the crystal plasticity model, further discussed in Section 3.2.

In addition to grain boundaries, also small particle inclusions may serve as sites for initiation of fatigue damage. This is for example observed in sheets of wrought Al6082-T6 in [23]. Such inclusions are also observed in forged Al6082 in [20] and in cast Al6082 in [35]. In contrast, particle inclusions or fatigue crack initiation due to particles could not be detected in the high-cycle fatigue experiments on wrought Al6082-T5 studied in [42]. Second-phase particles with sizes typically around 2 μm were found in the material presently under consideration. These particles contribute to give the high yield strength of this alloy in the T6 condition, while the small size relative to the grain size most likely means that the influence on fatigue crack initiation is minor. The main causes for microstructure heterogeneities appear to be the significantly elongated grain morphologies, due to the extrusion process, the crystallographic texture, and the presence and character of grain boundaries. Based on these observations, this study focuses on the influence of texture and grain boundary structure on the microstructure conditions for fatigue crack initiation in the vicinity of surface notches.

3 Crystal plasticity model and calibration

3.1 Constitutive model

The crystal plasticity model employed in the present work was introduced in [21] and the main components are summarized here for completeness. The starting point is a multiplicative split of the deformation gradient $\boldsymbol{F}$ into elastic and plastic components, which provide

$$\boldsymbol{F} = \boldsymbol{F}^{\mathrm{e}}\boldsymbol{F}^{\mathrm{p}} \tag{1}$$

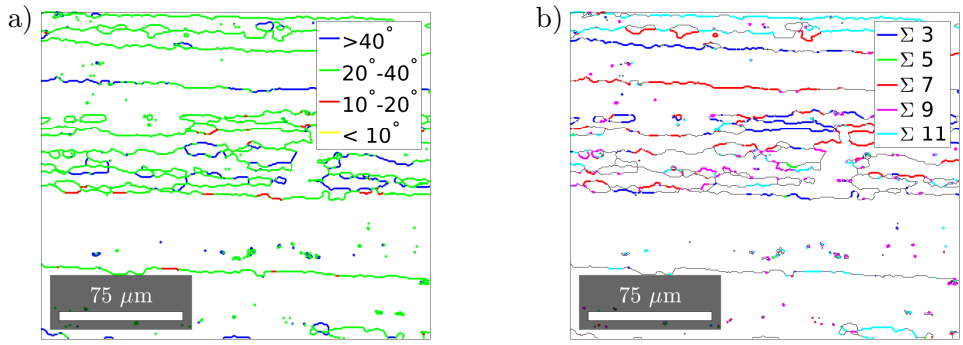

Figure 5: Grain boundary character in the extruded material. a) The majority of the grain boundaries are high-angle interfaces. b) Coincidence Site Lattice (CSL) correspondence, revealing presence of, e.g., Σ3 twin boundaries.

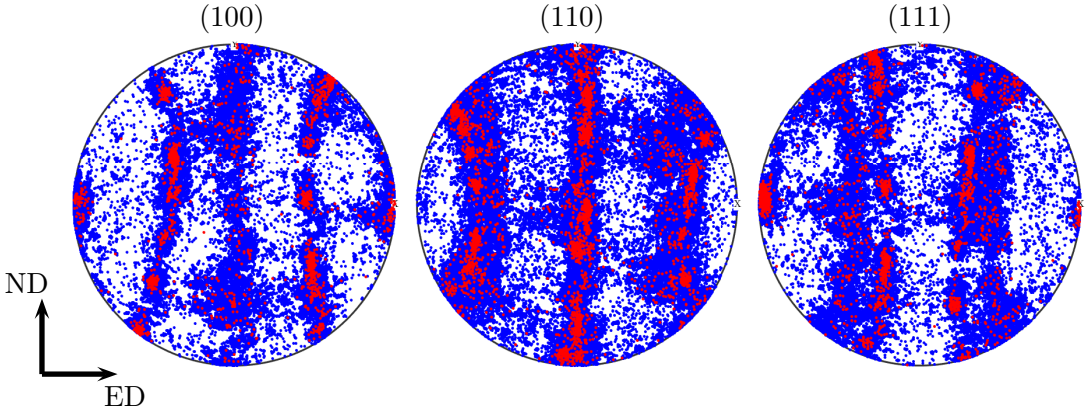

Figure 6: Pole figures showing the orientations of the crystals in the extruded material. ED is the extrusion direction. Blue dots represent the full set of 138 842 EBSD measurements and red dots show the subset of 500 randomly selected orientations which are used as a representative texture in the calibration of the crystal plasticity model.

Table 1: Designations of the slip planes and directions constituting the 12 $\{111\}\langle 110\rangle$ slip systems in a FCC crystal. The labels refer to the Schmid and Boas designations [41].

Number (α)	**Label**	**Slip system**	**Number** (α)	**Label**	**Slip system**
1	A2	$(\bar{1}11)\,[0\bar{1}1]$	4	B2	$(111)\,[0\bar{1}1]$
2	A3	$(\bar{1}11)\,[101]$	5	B4	$(111)\,[\bar{1}01]$
3	A6	$(\bar{1}11)\,[110]$	6	B5	$(111)\,[\bar{1}10]$
7	C1	$(\bar{1}\bar{1}1)\,[011]$	10	D1	$(1\bar{1}1)\,[011]$
8	C3	$(\bar{1}\bar{1}1)\,[101]$	11	D4	$(1\bar{1}1)\,[\bar{1}01]$
9	C5	$(\bar{1}\bar{1}1)\,[\bar{1}10]$	12	D6	$(1\bar{1}1)\,[110]$

This decomposition corresponds to a separation between the elastic stretch and rigid-body rotation of the crystal lattice, described by $\boldsymbol{F}^{\mathrm{e}}$ and plastic slip deformation in the undeformed lattice, described by $\boldsymbol{F}^{\mathrm{p}}$. The evolution of plastic deformation can be stated as

$$\dot{\boldsymbol{F}}^{\mathrm{p}} = \boldsymbol{l}^{\mathrm{p}}\boldsymbol{F}^{\mathrm{p}} \tag{2}$$

where $\boldsymbol{l}^{\mathrm{p}}$ is the plastic velocity gradient and where a superposed dot $\dot{(\cdot)}$ indicates differentiation with respect to time. It is assumed that plastic deformation is isochoric, whereby $\det(\boldsymbol{F}^{\mathrm{p}}) = 1$ and $\mathrm{tr}(\boldsymbol{l}^{\mathrm{p}}) = 0$. Here $\det(\cdot)$ and $\mathrm{tr}(\cdot)$ denote the determinant and the trace of a tensorial quantity, respectively. Any volume change J between the reference and deformed configurations will be purely elastic and $J = J^{\mathrm{e}} = \det(\boldsymbol{F}^{\mathrm{e}})$ can be assumed.

The plastic velocity gradient is directly related to the slip rates on the different slip systems in the crystal under consideration. The slip systems comprise the close-packed planes and directions in the lattice and as a FCC-structured material is presently under consideration, the 12 slip systems are found among the $\{111\}\langle 110\rangle$ planes and directions, cf. Table 1. Each slip system $\alpha \in [1, 12]$ can in the intermediate configuration be defined by the two orthonormal vectors $\boldsymbol{M}_\alpha$ and $\boldsymbol{N}_\alpha$, defining the slip direction and the slip plane normal, respectively. The velocity gradient is evaluated from a superposition of the slip rates $\dot{\gamma}_\alpha$ on the individual slip systems by performing the summation

$$\boldsymbol{l}^{\mathrm{p}} = \sum_{\alpha=1}^{12} \dot{\gamma}_\alpha \boldsymbol{M}_\alpha \otimes \boldsymbol{N}_\alpha \tag{3}$$

The effective plastic strain, or slip, rate can be found as

$$\dot{\varepsilon}^{\mathrm{p}}_{\mathrm{eff}} = \left(\frac{2}{3}\boldsymbol{l}^{\mathrm{p}} : \boldsymbol{l}^{\mathrm{p}}\right)^{1/2} \tag{4}$$

If integrated in time, $\dot{\varepsilon}^{\mathrm{p}}_{\mathrm{eff}}$ provides the accumulated plastic slip on all slip systems.

The slip rates are evaluated from the power law

$$\dot{\gamma}_\alpha = \dot{\gamma}_0 \left(\frac{|\tau_\alpha - b_\alpha|}{G^r_\alpha}\right)^m \mathrm{sign}\,(\tau_\alpha - b_\alpha) \tag{5}$$

where $\dot{\gamma}_0$ is a reference slip rate, G_α^r the slip resistance on slip system α and m a parameter controlling the rate sensitivity. In addition, τ_α and b_α is the resolved shear stress and back stress on system α, respectively. Eq. (5) can be integrated in time to obtain the accumulated slip γ_α on each slip system. The resolved shear stress is provided by

$$\tau_\alpha = \boldsymbol{M}_\alpha \boldsymbol{\Sigma}^{\mathrm{e}} \boldsymbol{N}_\alpha \tag{6}$$

The Mandel stress $\boldsymbol{\Sigma}^{\mathrm{e}}$ appears in eq. (6) and is evaluated as $\boldsymbol{\Sigma}^{\mathrm{e}} = \boldsymbol{C}^{\mathrm{e}} \boldsymbol{S}^{\mathrm{e}}$, where $\boldsymbol{S}^{\mathrm{e}}$ is the second Piola-Kirchhoff stress tensor in the intermediate configuration and $\boldsymbol{C}^{\mathrm{e}} = \boldsymbol{F}^{\mathrm{e}\mathrm{T}} \boldsymbol{F}^{\mathrm{e}}$ the elastic right Cauchy-Green deformation tensor. The transpose of a tensorial quantity is denoted by $(\cdot)^{\mathrm{T}}$.

The elasticity in the model is taken as isotropic, which is also the approach adopted for crystal plasticity modeling in, e.g., [13–15, 48]. Possible influence of anisotropic elasticity on constraining microplasticity is discussed in [46]. A Neo-Hookean elastic behavior is assumed in the present model, allowing the second Piola-Kirchhoff stress tensor to be stated as

$$\boldsymbol{S}^{\mathrm{e}} = \frac{\kappa}{2}\left(J^2 - 1\right)\boldsymbol{C}^{\mathrm{e}-1} + \mu J^{-2/3}\left(\boldsymbol{I} - \frac{1}{3}\mathrm{tr}\left(\boldsymbol{C}^{\mathrm{e}}\right)\boldsymbol{C}^{\mathrm{e}-1}\right) \tag{7}$$

where $(\cdot)^{-1}$ denotes the inverse of a tensor, $\boldsymbol{I}$ is the second-order identity tensor and κ and μ are the bulk and shear modulus, respectively.

Taking advantage of $\boldsymbol{M}^\alpha$ and $\boldsymbol{N}^\alpha$ being orthonormal, the resolved shear stress τ^α can be evaluated from

$$\tau_\alpha = \mu \boldsymbol{M}_\alpha \hat{\boldsymbol{C}}^{\mathrm{e}} \boldsymbol{N}_\alpha \tag{8}$$

where $\hat{\boldsymbol{C}}^{\mathrm{e}} = J^{-2/3}\boldsymbol{C}^{\mathrm{e}}$ is the isochoric part of the elastic right Cauchy-Green tensor. Further, the second Piola-Kirchhoff stress tensor $\boldsymbol{S}$ can be obtained from $\boldsymbol{S}^{\mathrm{e}}$ in the intermediate configuration from $\boldsymbol{S} = \boldsymbol{F}^{\mathrm{p}-1}\boldsymbol{S}^{\mathrm{e}}\boldsymbol{F}^{\mathrm{p}-\mathrm{T}}$ and the Cauchy stress tensor is obtained from

$$\boldsymbol{\sigma} = \frac{1}{J}\boldsymbol{F}\boldsymbol{S}\boldsymbol{F}^{\mathrm{T}} \tag{9}$$

The slip resistance G_α^r was introduced in eq. (5) and can, following e.g. [7, 34], be described by

$$G_\alpha^r = G_0 + G_\alpha, \qquad G_\alpha = Q\sum_{\beta=1}^{12} h_{\alpha\beta} g_\beta \tag{10}$$

Lattice friction is defined by the constant G_0 and the isotropic hardening behavior is controlled by the parameter Q and the hardening matrix $h_{\alpha\beta} = \delta_{\alpha\beta} + q\left(1 - \delta_{\alpha\beta}\right)$, describing slip system interaction. The parameter q controls the ratio between self-hardening on individual slip systems and latent hardening by slip system interaction. The back stress introduced in eq. (5) is described by

$$b_\alpha = H\nu_\alpha \tag{11}$$

where H is a kinematic hardening parameter. The slip-rate controlling variables g_α and ν_α evolve according to

$$\begin{aligned} \dot{g}_\alpha &= (1 - Bg_\alpha)\,\frac{|\tau_\alpha - b_\alpha|}{G_\alpha^r}\dot{\gamma}_\alpha \\ \dot{\nu}_\alpha &= \dot{\gamma}_\alpha - R\nu_\alpha|\dot{\gamma}_\alpha| \end{aligned} \tag{12}$$

where the parameters B and R control the saturation behavior of g_α and ν_α, respectively.

The mechanical dissipation is evaluated as

$$\mathcal{D} = \sum_{\alpha=1}^{12}\left(|\tau_\alpha - b_\alpha| - \frac{|\tau_\alpha - b_\alpha|}{G_\alpha^{\mathrm{r}}}G_\alpha + B\frac{|\tau_\alpha - b_\alpha|}{G_\alpha^{\mathrm{r}}}G_\alpha g_\alpha + \frac{H}{R}\left(b_\alpha\right)^2\right)|\dot{\gamma}_\alpha| \geq 0 \tag{13}$$

The dissipation in eq. (13) will always be positive since it holds that $G_\alpha^{\mathrm{r}} \geq G_\alpha$ according to eq. (10). Next, the rate of plastic work is obtained as

$$\dot{W}^{\mathrm{p}} = \sum_{\alpha=1}^{12}\tau_\alpha\dot{\gamma}_\alpha \tag{14}$$

Finally, by combining eqs. (13) and (14), the change in stored energy is provided by

$$\dot{E} = \dot{W}^{\mathrm{p}} - \mathcal{D} \tag{15}$$

3.2 Calibration

Calibration of the crystal plasticity model is performed using a single integration point in which the deformation is controlled by prescribing the deformation gradient $\boldsymbol{F}$. For isochoric uniaxial tensile/compressive deformation this can be achieved by prescribing

$$\boldsymbol{F} = \lambda\boldsymbol{e}_1 \otimes \boldsymbol{e}_1 + \frac{1}{\sqrt{\lambda}}\left(\boldsymbol{e}_2 \otimes \boldsymbol{e}_2 + \boldsymbol{e}_3 \otimes \boldsymbol{e}_3\right) \tag{16}$$

where $\boldsymbol{e}_i$ are the orthonormal unit base vectors and the parameter λ is incremented or decremented in each step, depending on if tension or compression is desired. The Cauchy stress tensor is obtained from eq. (9) and, as an example, the stress component in the x-direction can be evaluated as $\sigma = \boldsymbol{e}_1\boldsymbol{\sigma}\boldsymbol{e}_1$. The logarithmic strain is simply $\ln(\lambda)$.

A total of 500 grains are considered in the calibration simulations with orientations corresponding to the red markings in the pole figures in Fig. 6. These 500 orientations are a representative subset of the orientations mapped by EBSD in relation to the experiments. It is worth noting that crystallographic texture is otherwise often disregarded in calibrations of crystal plasticity models, which may induce significant errors.

In [1], the response of the extruded Al6082-T6 material at different load amplitudes was established by incremental step testing, cf. [27]. The measurements were fitted by the Ramberg-Osgood relation

$$\frac{\Delta\varepsilon}{2} = \frac{\Delta\sigma}{2E} + \left(\frac{\Delta\sigma}{2K}\right)^{1/n} \tag{17}$$

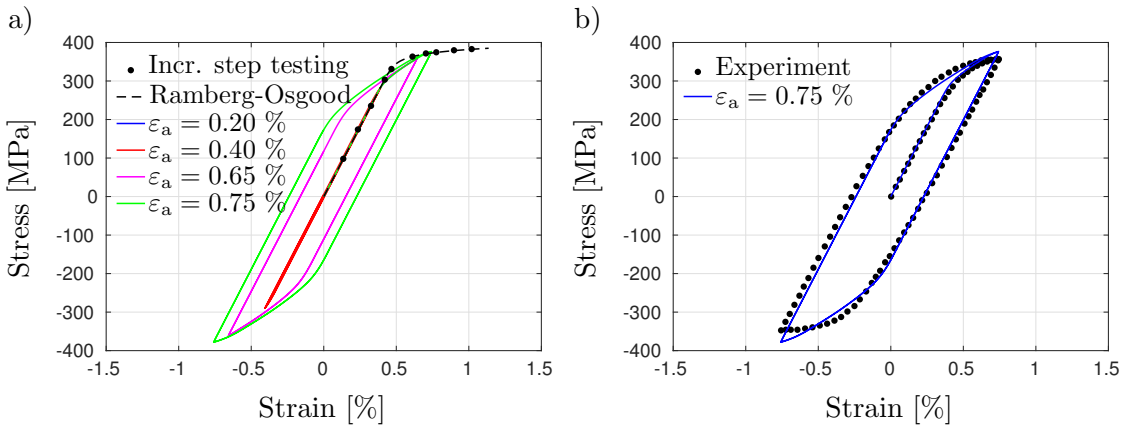

Figure 7: a) Calibrated model response (colored solid lines) at four different strain amplitudes ε_a, compared to experimental data from incremental step testing (black dots) fitted by the Ramberg-Osgood formula in eq. (17) (dashed black line). b) Validation of the calibration by direct comparison between test data and simulation output for a full load cycle at $\varepsilon_a = 0.75\%$. The experimental data in both figures is taken from [1].

in which $\Delta\varepsilon$ and $\Delta\sigma$ are the strain and stress ranges, $E = 72.5$ GPa the experimentally determined elastic modulus and K and n parameters in the Ramberg-Osgood formula. A good fit of the experimental data was found for $K = 458$ and $n = 0.034$, as shown in Fig. 7.

The crystal plasticity model parameters are fitted to the incremental step test data, as represented by the Ramberg-Osgood fit, by using Matlab and the built-in "fminsearch" function. The elastic parameters in the crystal plasticity model were evaluated as $\mu = 26.8$ GPa and $\kappa = 80.6$ GPa, using a Poisson ratio of 0.35, and the latent hardening parameter is set to $q = 1.4$, following e.g. [39]. The rate sensitivity of aluminum is relatively low and the rate sensitivity parameter m is set to 100, in line with [19, 25].

The calibrated values of the remaining parameters are provided in Table 2 and the calibrated model response is shown in Fig. 7a together with the experimental data. To further verify the calibration, a load cycle obtained from the crystal plasticity model is shown together with a stabilized hysteresis curve, obtained in the constant amplitude experiments in

Table 2: Calibrated crystal plasticity model parameters.

Parameter	**Value**	**Description**
G_0	205 MPa	Lattice friction
$\dot{\gamma}_0$	0.04 1/s	Reference slip rate
Q	1 MPa	Isotropic hardening parameter
B	14	Isotropic hardening parameter
H	100 kPa	Kinematic hardening parameter
R	10	Kinematic hardening parameter

[1], in Fig. 7b.

3.3 Simulation model

In order to investigate the microstructure influence in the vicinity of the notches at which fatigue crack initiation was found to occur [1], representative numerical models are constructed as shown in Fig. 8. As indicated in Fig. 8, the notch geometries in each of the two test specimens (specimen 1 and 2) are denoted by "Notch A" and "Notch B", respectively. The simulation domains are 400×200 µm^2 and the geometry of the top boundary, i.e. the specimen surface, is obtained from the WLI-measured surface profiles shown in Fig. 1. A time-varying displacement of the left and right domain boundaries is prescribed to induce cyclic deformation. The boundary conditions are shown in Fig. 9. In correspondence with the experiments, also cf. Section 2, a strain range of 0.5 % is used for specimen 1 and a strain range of 0.4 % for specimen 2. A total of 20 load cycles are considered, which is in the order

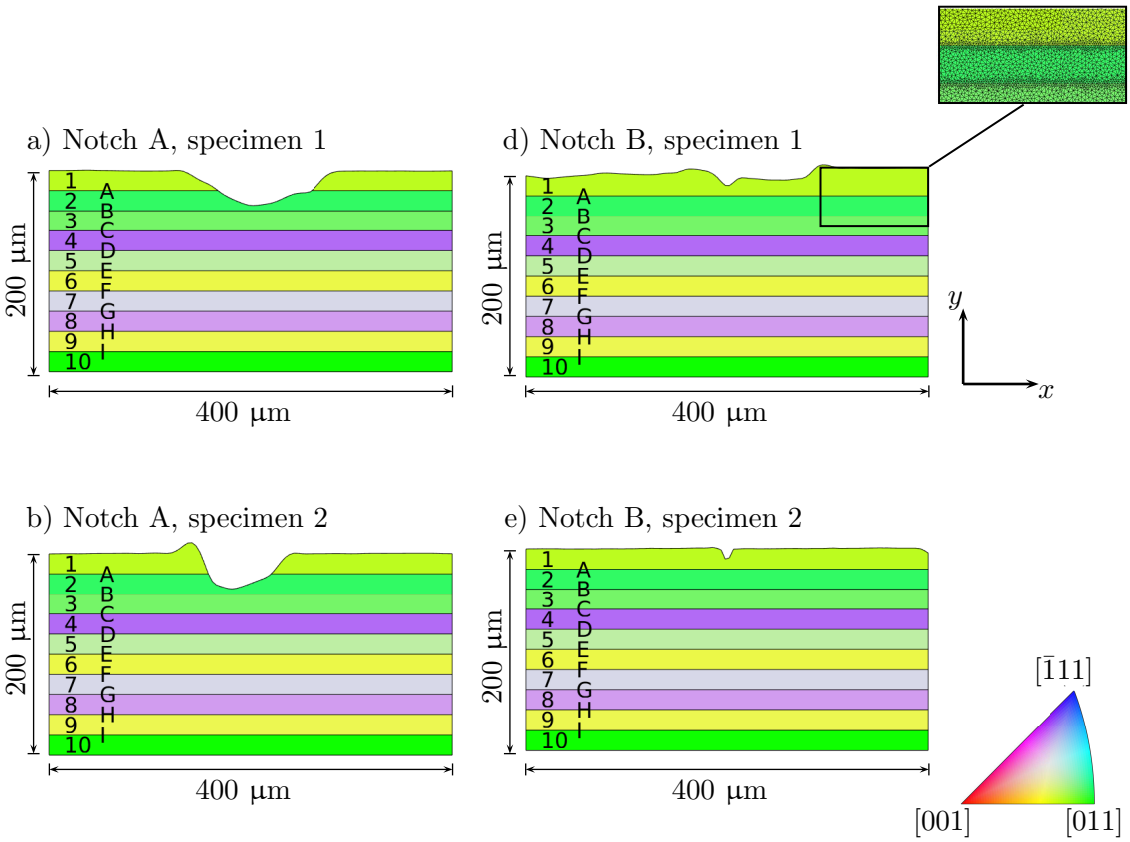

Figure 8: Notch geometries used in the simulations. The notches correspond to the surface mappings shown in Fig. 1 and the coloring indicate the grain orientations, cf. Fig. 4 and Table 3. The thickness of each grain, denoted by the numbers 1 . . . 10, is 20 µm and the grain boundaries are denoted by letters A. . .J, cf. Table 3. The finite element mesh discretization is illustrated by the top-right picture inlay.

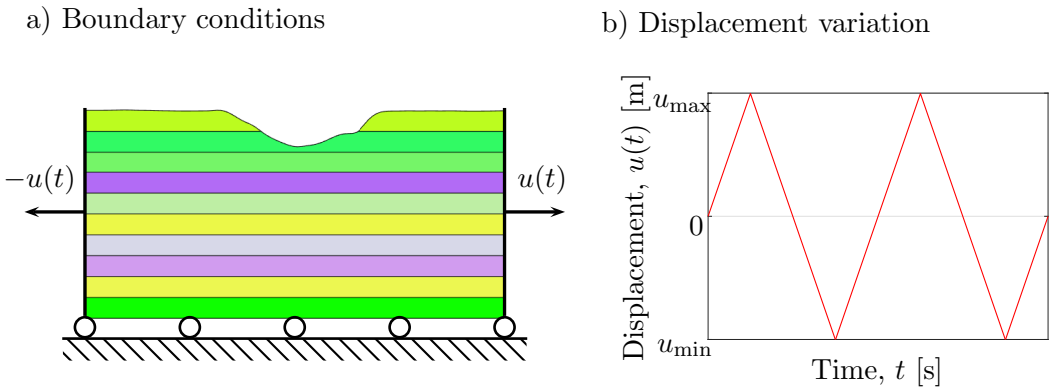

Figure 9: a) Boundary conditions used in the numerical simulations. b) Schematic illustration of the time-varying displacement imposed on the left and right boundaries of the model (in opposite directions).

of what is used in the crystal plasticity-based fatigue studies in [46, 50]. The computational domains are discretized by Delaunay triangularization, using approximately 60 000 triangular elements with linear interpolation. The mesh is refined along the top surface and along the grain boundaries. The mesh discretization is indicated by the inlay picture in Fig. 8. Plane strain conditions are assumed.

As indicated by the EBSD map in Fig. 4, the grain structure consists of lamellar grains which are elongated in the extrusion/loading direction. Unfortunately, EBSD maps are not available at each of the individual notches. Instead, the map in Fig. 4 is taken as being representative for the extruded material. Based on this, artificial grain structures are generated as shown by the orientation color-coding in Fig. 8. Each lamellar grain is 20 μm in thickness, motivated by the grain sizes observed in Fig. 4. The grain orientations are taken from the EBSD data and are provided in Table 3. This table also shows the misorientation and possible CSL correspondence for each of the grain boundaries in the model. It can be noted that boundaries G and J are of low-angle character and hence can be expected to only constitute minor barriers to slip while, for example, boundaries B and F are twin boundaries through which slip is significantly restricted. The grain orientations also indicate that the crystals tend to have the $\langle 111 \rangle$ axes, or to a lesser extent the $\langle 100 \rangle$ axes, parallel to the loading/extrusion direction.

In order to investigate the influence of microstructure variations beneath the notches, different variants of the grain stacking sequence are generated by a cyclic shift of the grain positions in the vertical direction, and subsequently evaluated. The grain ordering is shown by the grain and grain boundary labels in Fig. 8. The effect of this reordering is that the position of grains of different orientations and the position of the individual grain boundaries with respect to the near-notch region is altered.

Table 3: Grain orientations considered in the simulations, following the Euler-Bunge convention. The misorientation θ and possible CSL correspondence for each grain boundary is stated in the last two columns.

Grain	$(\varphi_1, \Phi, \varphi_2)$ [°]	**Boundary (grains)**	θ [°]	**CSL type**
1	(349, 33, 182)	A (1 and 2)	58.1	N.A.
2	(57, 43, 84)	B (2 and 3)	57.9	Σ3
3	(213, 94, 141)	C (3 and 4)	33.3	Σ7
4	(137, 119, 297)	D (4 and 5)	45.6	Σ19b
5	(321, 97, 304)	E (5 and 6)	41.7	N.A.
6	(8, 62, 273)	F (6 and 7)	57.9	Σ3
7	(311, 60, 342)	G (7 and 8)	4.1	Σ1
8	(312, 62, 158)	H (8 and 9)	57.2	N.A.
9	(87, 87, 242)	I (9 and 10)	18.2	N.A.
10	(87, 90, 224)	J (10 and 1)	12.8	Σ1

3.4 Fatigue initiation parameters

Different Fatigue Initiation Parameters (FIP) can be envisaged for investigating the conditions for fatigue crack initiation. In addition to monitoring the macroscopic stress concentration, i.e. the location of $\max(\sigma_{xx})$, four additional FIPs are examined in the present work. The first is based on the accumulated plastic strain, defined in eq. (4), and can be defined by

$$\mathrm{FIP}_{\varepsilon} = \varepsilon^{\mathrm{p}}_{\mathrm{eff}} \tag{18}$$

The second is based on the accumulated stored energy found in eq. (15), and is defined by

$$\mathrm{FIP}_{E} = E \tag{19}$$

The third FIP considered in the present study is based on a modification of the Fatemi-Socie parameter [17]. The Fatemi-Socie parameter is a macroscopic parameter of critical-plane type. It involves the maximum plastic shear strain which is accumulated in each cycle and the maximum normal stress on the plane where the maximum plastic shear range is found. Recognizing that fatigue crack initiation is intimately linked to local irreversible slip, the Fatemi-Socie criterion was recast in [8, 31] in terms of the maximum plastic slip $\Delta\gamma_\alpha$ being accumulated in slip system α during a cycle and the peak stress $\sigma_{\mathrm{n},\alpha}$, normal to the corresponding slip plane. Following [31], this modified Fatemi-Socie criterion appears as

$$\mathrm{FIP}_{\mathrm{FS}} = \max_{\alpha=1\ldots12} \left[\frac{1}{2} \Delta\gamma_\alpha \left(1 + k \frac{\sigma_{\mathrm{n},\alpha}}{\sigma_0} \right) \right] \tag{20}$$

where the usual choice of $k = 1/2$ is adopted here and where σ_0 is a reference strength. The latter parameter is in the present work set to $\sigma_0 = 382$ MPa, corresponding to the material's yield stress [1] and providing consistent units in eq. (20) as discussed in [17]. The parameter

$\mathrm{FIP}_{\mathrm{FS}}$ is evaluated for all slip systems $\alpha = 1 \ldots 12$ and the maximum at each finite element integration point in the mesh is monitored in the simulations.

Finally, also a FIP based on the Dang Van [11, 49] criterion is considered. This criterion is based on the combined influence of the shear stress acting on the individual slip planes and the hydrostatic stress. The criterion considers localized plastic activity in the microstructure of a material that is macroscopically kept in the elastic regime. Since it was introduced, the criterion has been repeatedly reinterpreted and employed in a range of studies on fatigue crack propagation in polycrystalline metals. Here, the formulation of the Dang Van criterion proposed in [5] is adopted to provide

$$\mathrm{FIP}_{\mathrm{DV}} = \max_{\alpha=1\ldots12} \left(\frac{\Delta\tau_\alpha}{2} \right) + k_{\mathrm{DV}} P_{\max} \tag{21}$$

where $\Delta\tau_\alpha$ is the range of the resolved shear stress on each slip system α and where $P_{\max} = \max\left(\mathrm{tr}\left(\boldsymbol{\sigma}\right)\right)/3$ is the peak hydrostatic pressure. In addition, k_{DV} is a parameter which is here set to $k_{\mathrm{DV}} = 0.2$, following [5].

As a comment on the presently adopted set of FIPs, it is noted that the macroscopic stress concentration is the classical indicator used for localization of fatigue damage initiation. In addition, the present study also consider the accumulated plastic slip which is used as FIP in, for example, [9, 16, 18, 29]. Further, deformation energy - either in terms of the dissipated or the stored energy - is, for example, considered in the studies presented in [26, 50]. In passing it may also be noted that a host of other FIPs have been suggested in the literature, such as the criteria by Crossland [10] and Matake [30]. Different FIPs are further discussed in [32, 43] in relation to crystal plasticity simulations of fatigue crack formation.

4 Results and discussion

In [1], the work which motivated the present study, the classical approach was taken by considering macroscopic stress concentrations for identification of the likely fatigue crack initiation sites. Fig. 10 shows the distribution of the normal stress component along the x-axis (being the loading/extrusion direction) and it is evident that the highest stress concentrations appear at the notch tip in all of the simulation scenarios under consideration. It is, however, again emphasized that in the experiments in [1], most fatigue failures were initiated at other locations than at the highest macroscopic stress concentration. Figs. 10 a and c indicate that the stress is higher in a larger region beneath the notches at which fatigue damage was initiated ("Notch A"), compared to the cases in Figs. 10b and d ("Notch B").

To further illustrate the differences in stress distribution at the notches, Fig. 11 shows how the σ_{xx} stress component - being the normal stress in the loading direction - varies along a vertical line extending from the notch tip and downwards. Fig. 11 shows the stress variation at the maximum strain amplitude $\varepsilon_{\max}$ in the last load cycle for each of the specimens. The results labeled with "FE" are stress variations evaluated in [1, 2] by elastic-plastic finite element modeling. The magnitude of the stresses obtained in [1, 2] are in Fig. 11 seen to be lower than

those obtained from the present crystal plasticity simulations. This difference can most likely be explained by different constitutive models being used and by axisymmetric conditions being adopted in [1, 2] while a smaller simulation domain and plane strain conditions are adopted here. In Fig. 11, it can also be noted that very steep stress gradients are found beneath notch B in both specimens (red lines). A considerably less steep gradient is found at notch A, representing the site of fatigue crack initiation, in each specimen (blue lines). In fact, whereas the stress beneath notch B drops to a lower and constant value of approximately 300 MPa within a single grain, the stress beneath notch A remains higher over three grains and across three grain boundaries. As fatigue was initiated at notch A, in each specimen, this can be taken as an indication of the impact of stress gradients on fatigue crack initiation in the material. Apparently, a less steep stress gradient appears beneath the notches where fatigue damage was initiated. This observation is in agreement with the classical studies on gradient effects at stress concentrations by Neuber [38] and Sibel and Stieler [44].

The distribution of the effective plastic strain, i.e. FIP_{ε} is shown in Fig. 12. Evidently, the maximum values of FIP_{ε} predict fatigue to be initiated at the notch tip in all cases. But it can be noted that the effective plastic strain maintains a non-zero value over a larger region beneath the notch tip in both Figs. 12a and c, being the notches where fatigue was initiated. This is consistent with the appearance of the stress gradients in Fig. 10 and Fig. 11.

The other fatigue initiation parameter under consideration is due to the stored energy, i.e.

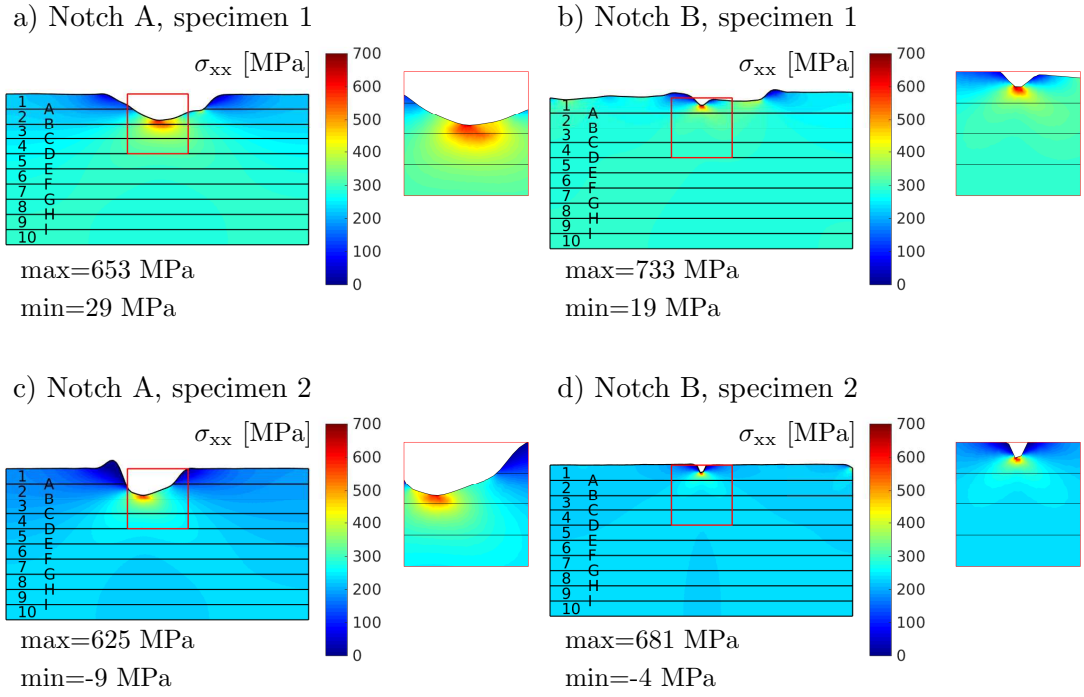

Figure 10: Normal stress in the loading direction, i.e. in the extrusion direction corresponding to the x-axis in Fig. 8, at the maximum strain amplitude in the last load cycle.

a) Specimen 1, stress at $\varepsilon = \varepsilon_{\max} = 0.25$ %

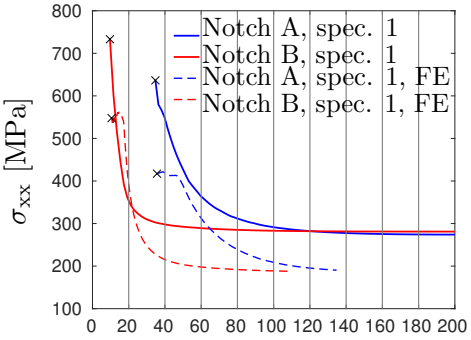

b) Specimen 2, stress at $\varepsilon = \varepsilon_{\max} = 0.20$ %

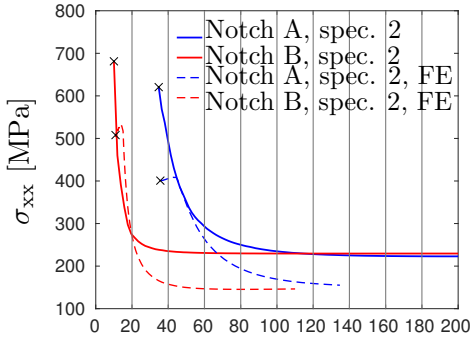

Figure 11: The variation of the σ_{xx} stress component - i.e. the stress component in the loading direction - along a vertical line below the notches, stress at the maximum strain amplitude. The notch tip is in each graph indicated by the symbol $\times$ and the positions of the grain boundaries are shown by the vertical gray lines. The different notches and specimens are defined in Fig. 8. The results labeled by "FE" are taken from the macroscopic elastic-plastic finite element simulations performed in [1]. a) Specimen 1. b) Specimen 2.

a) Notch A, specimen 1

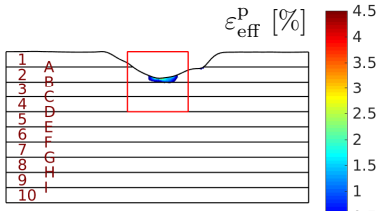

b) Notch B, specimen 1

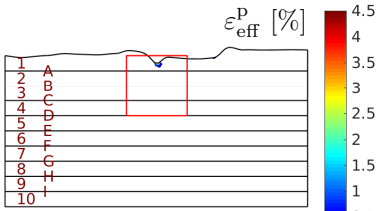

c) Notch A, specimen 2

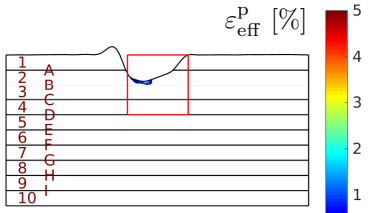

d) Notch B, specimen 2

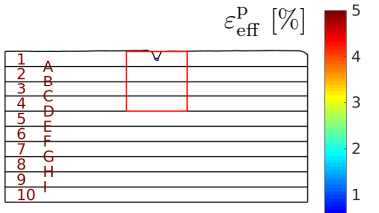

Figure 12: Distribution of the effective plastic strain, i.e. $\mathrm{FIP}_{\varepsilon}$ cf. eq. (18), at the maximum strain amplitude in the last load cycle.

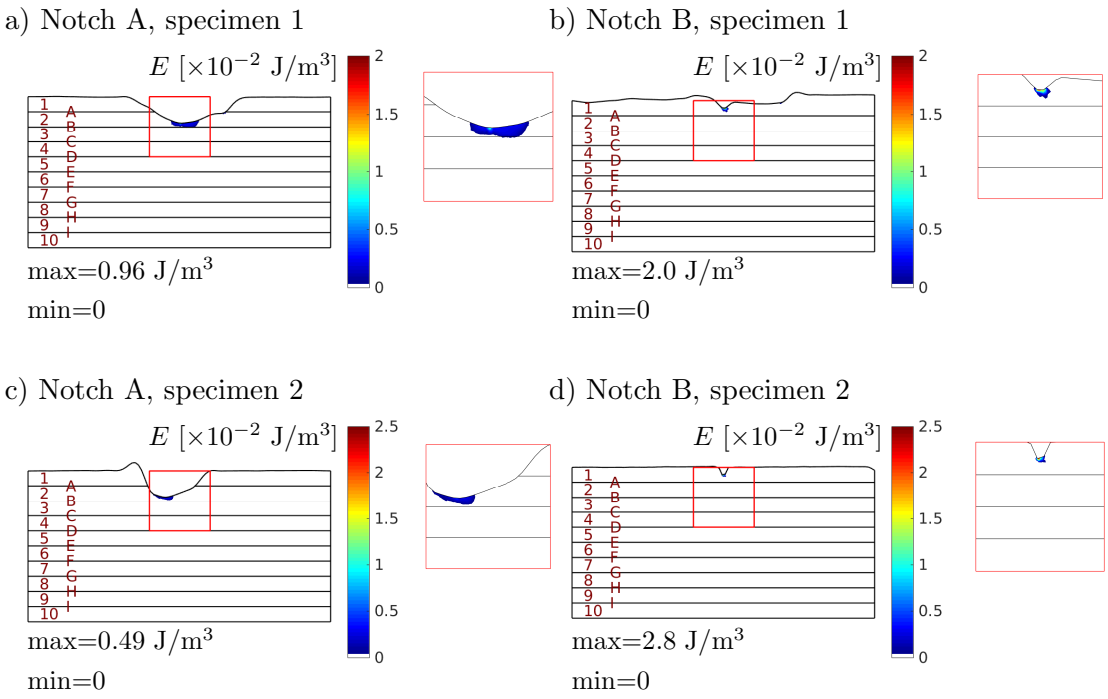

Figure 13: Distribution of stored energy, i.e. FIP_E cf. eq. (19), at the maximum strain amplitude in the last load cycle.

FIP_E. The distribution of this parameter is shown in Fig. 13. As with the previous fatigue damage indicators in terms of stress concentrations and effective plastic strain concentrations, also the stored energy FIP indicates fatigue crack initiation to take place close to the notch tip. But again - to no surprise as the stored energy is closely related to the plastic slip activity, i.e. to FIP_ε - it is noted that the region of non-zero stored energy extends further into the material beneath notch A in both specimens, compared to the situation at notch B. Just like the previous FIPs, also FIP_E indicates that fatigue damage was initiated beneath a notch where a relatively large volume of the material was influenced by the presence of a surface irregularity.

While stress concentrations are a macroscopic measure, although confined to singular notches in the present study, both FIP_ε and FIP_E relate to the extent of the local plastic deformation in the material. The latter two parameters do not, however, distinguish the relative slip activity among the different slip systems in a grain. If the maximum resolved shear stress τ_α is considered, a different view is provided. Fig. 14 shows the variation of the maximum resolved shear stress, evaluated for all slip systems in each grain. The maximum resolved shear stress reveals significantly more variation from one grain to another, than the previous parameters. This is an indication of the influence of the grain orientations close to a macroscopic stress concentration.

Another view of the the slip activity is found when looking at the distribution of the

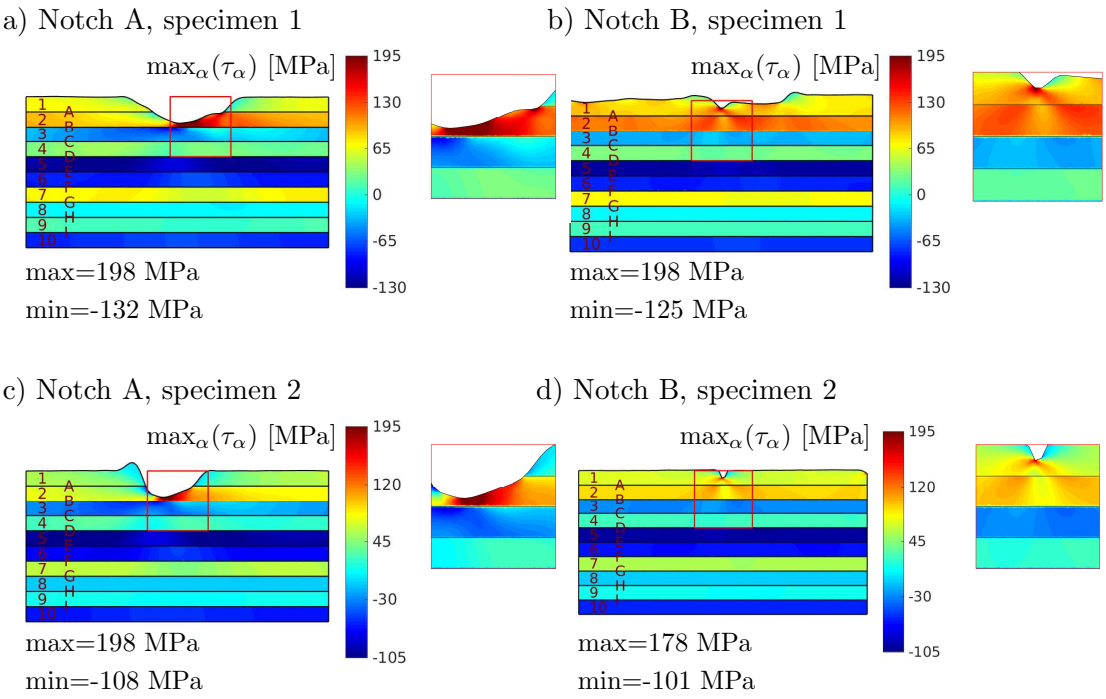

Figure 14: Maximum resolved shear stress on all slip systems in each grain at the maximum strain amplitude in the last load cycle, cf. eq. (8).

maximum plastic slip on all slip systems in each grain, cf. eq. (5), shown in Fig. 15. It is interesting to note that not only the spatial extent of the region with non-zero plastic slip, but also the *magnitude* of $\max_\alpha(\gamma_\alpha)$ is higher close to notch A, being the notch at which fatigue damage was initiated.

In passing, it can also be noted that the presence of the $\Sigma 3$ twin boundary B - through which slip propagation is difficult - influences the shape of the non-zero regions in, e.g., Figs. 12, 13 and 15. This is especially true for notch A, having the notch tip adjacent to grain boundary B.

Next, attention is turned to the $\mathrm{FIP_{FS}}$ parameter, which is based on a modified Fatemi-Socie criterion and which connect the maximum slip on each slip system with the normal stress acting on the same system, cf. eq. (20). The distribution of this parameter in the two simulated test specimens is shown in Fig. 16. Since $\mathrm{FIP_{FS}}$ is closely related to the local slip activity, it can be noted that the distribution of maximum slip in Fig. 15 is more or less identical to the distribution of $\mathrm{FIP_{FS}}$ in Fig. 16, indicating the influence of the slip system normal stress $\sigma_{\mathrm{n},\alpha}$ on the distribution to be minor (although the magnitude is affected). The influence of the normal stress component is influenced by the choices of the parameters k and σ_0 as seen in eq. (20). Different parameter choices are investigated and indicate the distribution of $\mathrm{FIP_{FS}}$ to be quite insensitive to particular values of k and σ_0.

Finally, the Dang Van criterion in terms of $\mathrm{FIP_{DV}}$ - defined in in eq. (21) - is considered.

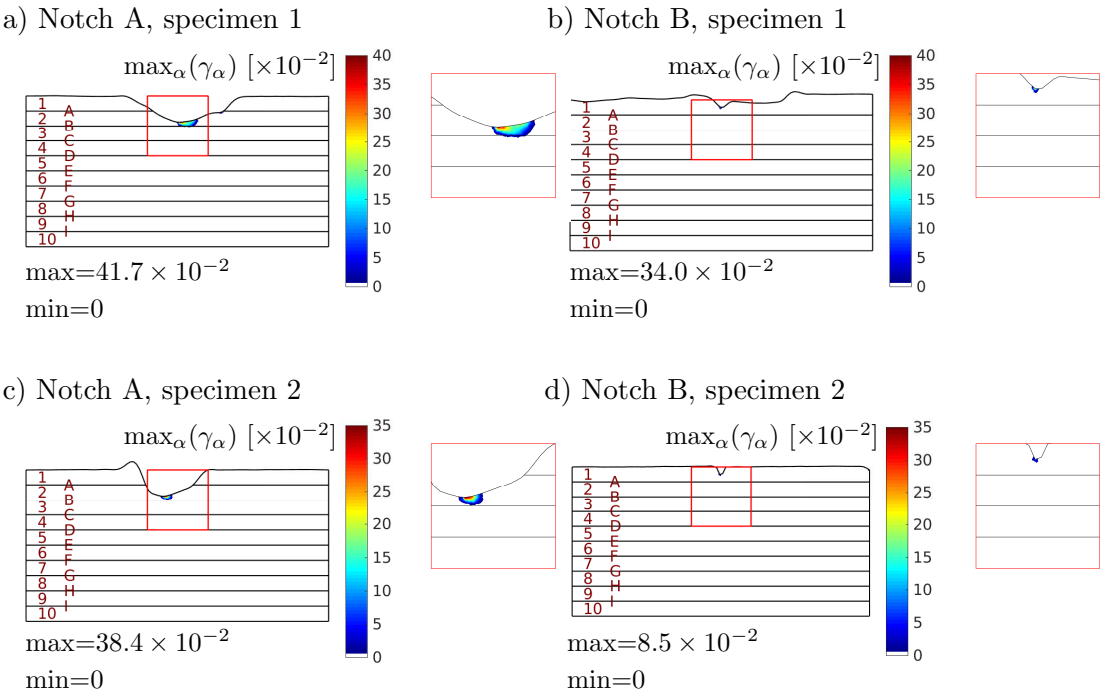

Figure 15: Maximum plastic slip, evaluated on all 12 slip systems in each grain, at the maximum strain amplitude in the last load cycle, cf. eq. (5).

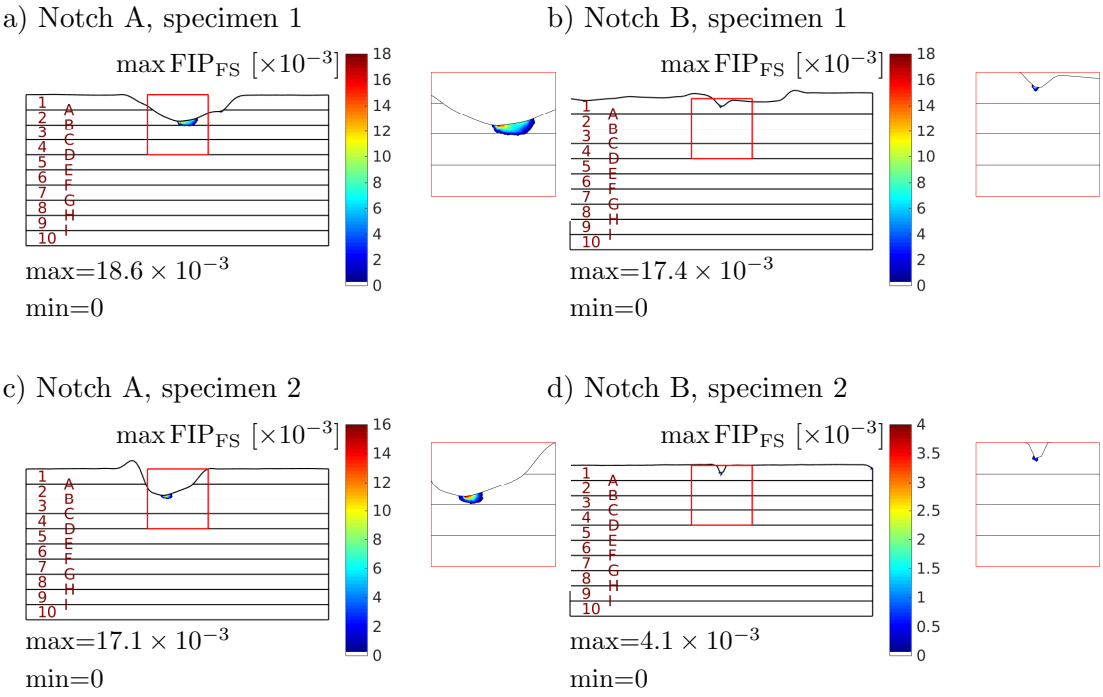

Figure 16: Distribution of the fatigue initiation parameter $\mathrm{FIP_{FS}}$ at the maximum strain amplitude in the last load cycle, cf. eq. (20).

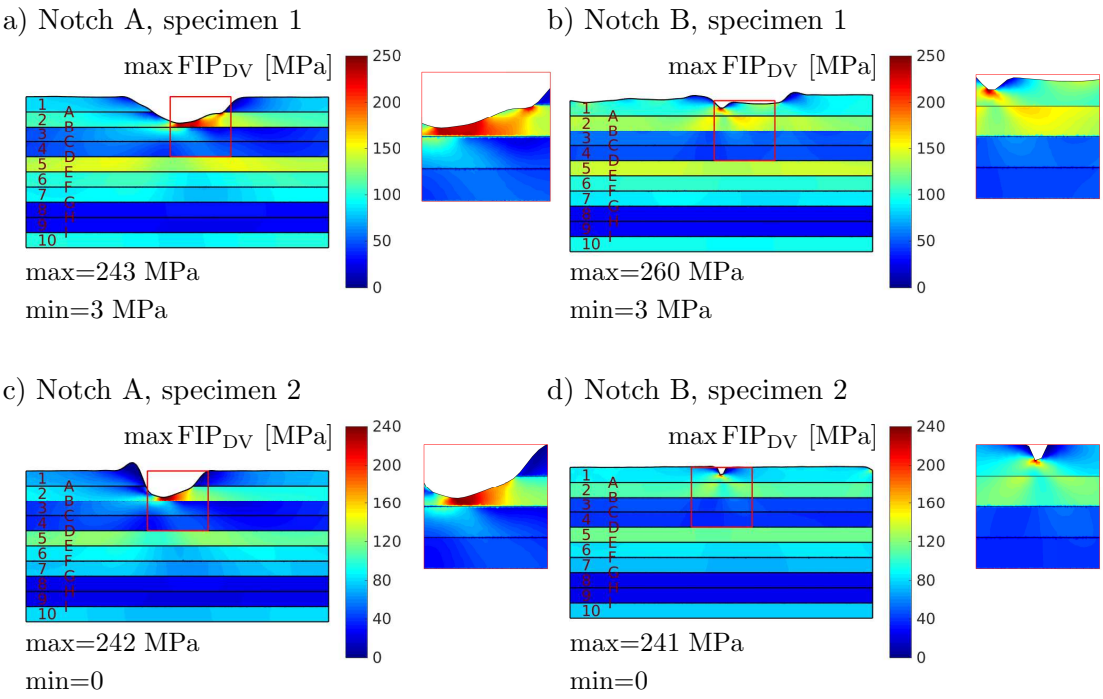

Figure 17: Distribution of the fatigue initiation parameter $\mathrm{FIP_{DV}}$ in the last load cycle, cf. eq. (21).

This FIP does not involve the slip itself, as do $\mathrm{FIP_{FS}}$, but is a purely stress-based measure. The distribution of $\mathrm{FIP_{DV}}$ is shown in Fig. 17. It can be noted that for the microstructures shown in Fig. 17, $\mathrm{FIP_{DV}}$ is of comparable magnitude in both notch A and B in the respective specimen. However, as was the case with $\mathrm{FIP_{FS}}$, the region holding high values of $\mathrm{FIP_{DV}}$ is larger beneath notch A, compared to notch B. Although notch A is indicated to be the more likely site for fatigue crack initiation in specimen 2, both by $\mathrm{FIP_{FS}}$ and $\mathrm{FIP_{DV}}$, this is not the case for specimen 1. It could be argued that perhaps $\mathrm{FIP_{DV}}$ is a more relevant FIP to use in the current settings where the extent of plasticity is quite limited.

To further investigate the influence of different grain structures, cyclic permutations of the assumed grain stacking sequence are investigated. The resulting differences in the distribution of $\mathrm{FIP_{FS}}$ in specimens 1 and 2 are shown in Fig. 18 and Fig. 19, respectively. All cyclic permutations of the grain stacking sequence were investigated, but only those which provided magnitudes of $\mathrm{FIP_{FS}}$ greater than an assumed numerical precision of 10^{-16} are shown. In a similar manner, the same cyclically permuted grain structures are also used to evaluate the distribution of $\mathrm{FIP_{DV}}$, as shown in Fig. 20 and Fig. 21 for specimens 1 and 2, respectively.

While the previous simulation results quite consistently put the location of the different FIP maxima at the notch tip, the results in Figs. 18-19 are more scattered. In Fig. 18a, the maximum value is beneath the notch tip, at grain boundary A in the material's interior. Comparing Figs. 18a and b, it can be noted that the magnitude of $\mathrm{FIP_{FS}}$ is higher at notch

A than at notch B. This indicates preferred fatigue crack initiation at notch A rather than at notch B, in agreement with the experiments. The same holds in Fig. 18c, showing a maximum at grain boundary J beneath notch A, although at considerably lower magnitudes of $\mathrm{FIP_{FS}}$. In Figs. 18e and f, as well as g and h, the situation is changed in the sense that notch B exhibits higher values of $\mathrm{FIP_{FS}}$ compared to notch A. Using $\mathrm{FIP_{FS}}$ as an indicator for fatigue initiation, it is evident that variations in the grain structure may quite drastically relocate the likely fatigue crack initiation site.

In Figs. 18a and c, the critical domains are in the material's interior and indicate regions for fatigue crack initiation which differ from the notch tip which is predicted by the macroscopic stress concentration, FIP_E and FIP_ε.

Fig. 19 shows the distribution of $\mathrm{FIP_{FS}}$ in specimen 2. Since this specimen is exposed to a lower load amplitude than specimen 1, it is to no surprise that the magnitudes of the slip-dependent $\mathrm{FIP_{FS}}$ parameter are smaller, compared to in specimen 1. In addition, the size of the non-zero regions in Fig. 19 are smaller than those seen in Fig. 18. Still, the same tendencies as those found for specimen 1 are also seen for specimen 2 in Fig. 19. For example, depending on the ordering of the grains, the highest values of $\mathrm{FIP_{FS}}$ can be found either at notch A (Fig. 19a and c) or at notch B (Fig. 19f and h). This again indicates that the microstructure conditions can provide an explanation for fatigue crack initiation at notch A rather than at notch B, as seen in the experiments.

The distribution of $\mathrm{FIP_{DV}}$ in specimen 1 is shown in Fig. 20. In the microstructures depicted in figures a-b and c-d in Fig. 20, notch A holds a significantly higher value of $\mathrm{FIP_{DV}}$, compared to notch B. The opposite is true, however, for the microstructures in figures e-f and g-h in Fig. 20. These trends are consistent with the results based on $\mathrm{FIP_{FS}}$ in Fig. 18. Turning to specimen 2, the distribution of $\mathrm{FIP_{DV}}$ is shown in Fig. 21. Again, higher values of $\mathrm{FIP_{DV}}$ are found at notch A compared to notch B in Fig. 21 a-b as well as in Fig. 21c-d. As for specimen 1, the opposite holds for figures e-f and g-h in Fig. 21. However, also for specimen 2 the notch having the highest value of $\mathrm{FIP_{DV}}$ coincides with the results based on $\mathrm{FIP_{FS}}$. Apparently, for both specimens 1 and 2, the two FIPs carry a certain degree of consistency in pointing out the most likely site for fatigue crack initiation in each simulated scenario. In addition, as is the case with $\mathrm{FIP_{FS}}$, also $\mathrm{FIP_{DV}}$ maintain high values in a larger region beneath notch A compared to notch B.

The crystal plasticity simulations agree with the elastic-plastic finite element results in [1, 2] by positioning the more severe stress concentration at notch B and not at notch A. However, as shown in Fig. 11 the stress distribution and the stress gradient is significantly different between the two notches. These results indicate notch A to be the more likely fatigue crack initiation site, in accordance with the experiments.

Considering the two FIPs based on effective plastic strain and stored energy, the highest values are found at the tip of notch B in each specimen. But the non-zero regions of these FIPs are larger near notch A.

Turning to the plastic slip activity and the magnitude of the resolved shear stress, notch A

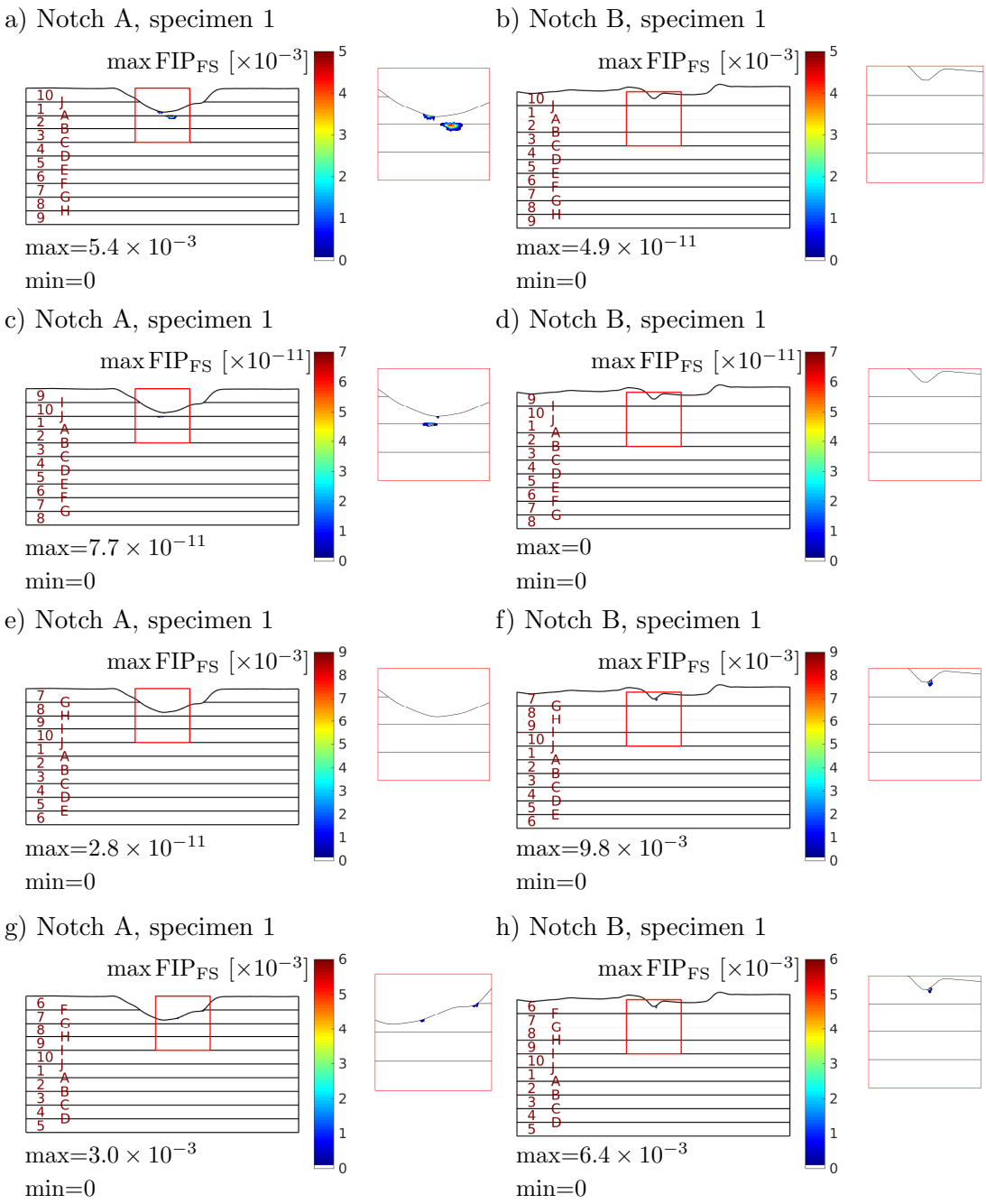

Figure 18: Distribution of FIP_{FS} in specimen 1 depending on the ordering of the grains. The results are obtained at the maximum strain amplitude in the last load cycle. Note that the magnitudes indicated by the color legends differ.

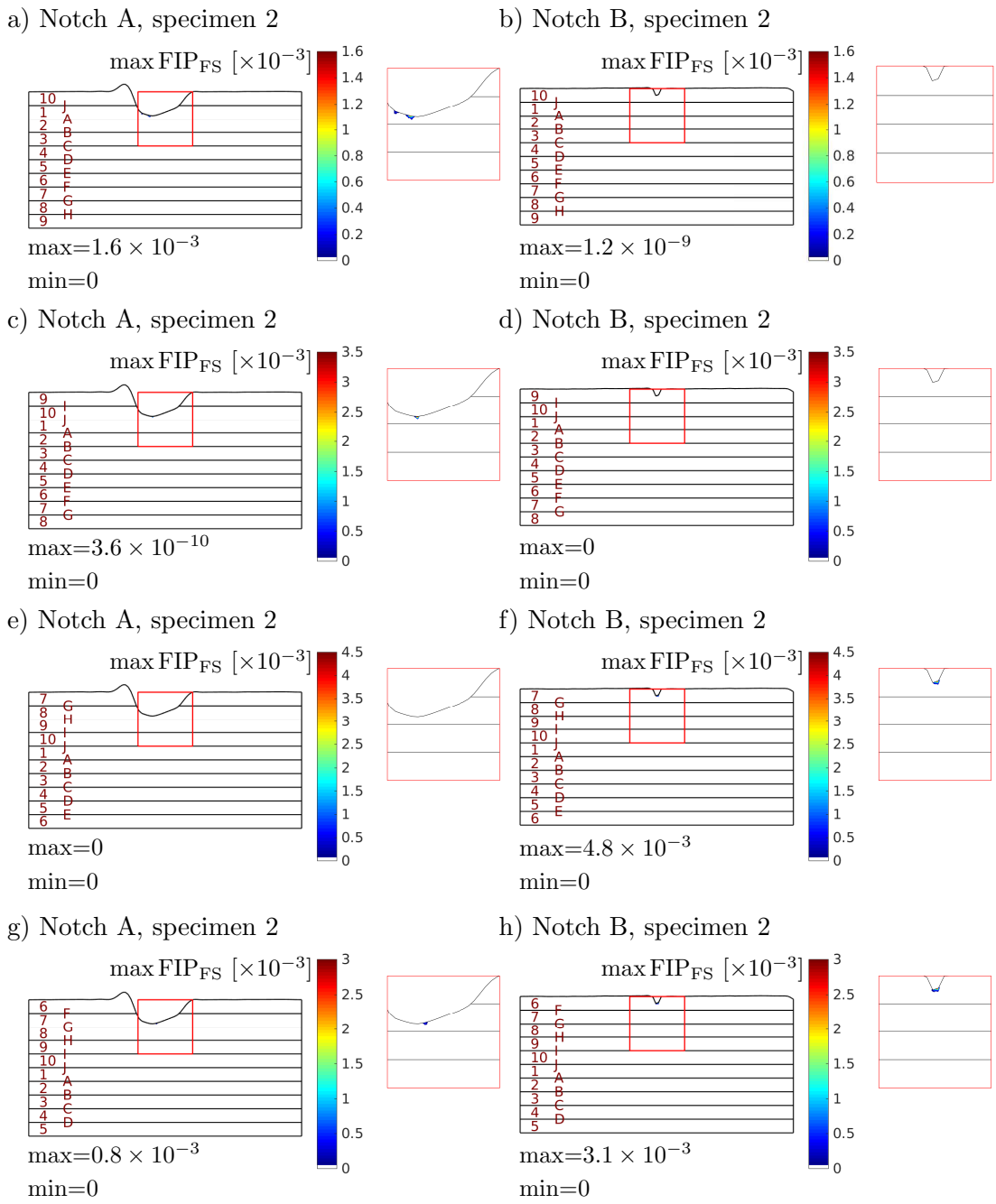

Figure 19: Distribution of FIP_{FS} in specimen 2 depending on the ordering of the grains. The results are obtained at the maximum strain amplitude in the last load cycle. Note that the magnitudes indicated by the color legends differ.

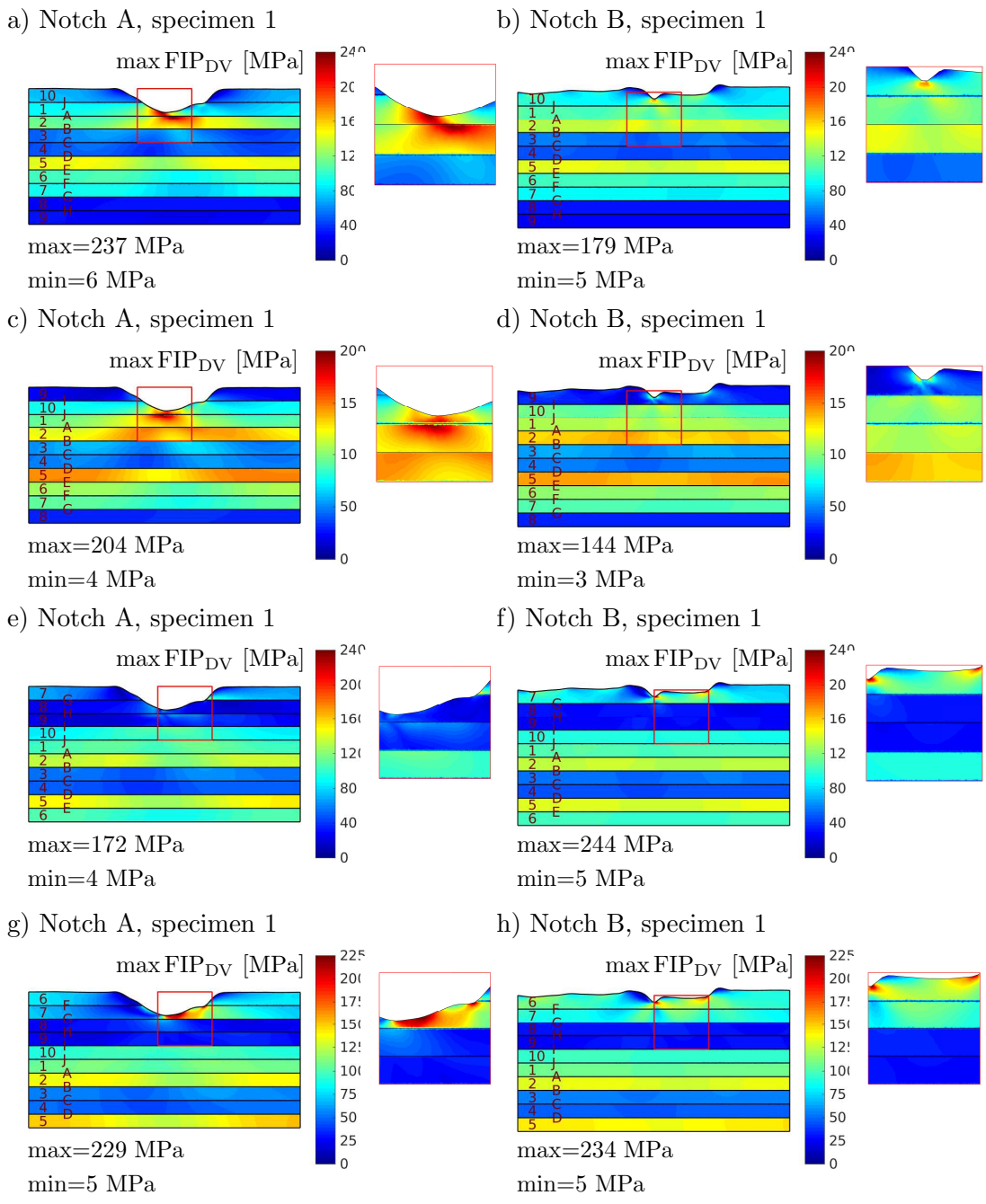

Figure 20: Distribution of FIP$_{DV}$ in specimen 1 depending on the ordering of the grains. The results are obtained in the last load cycle.

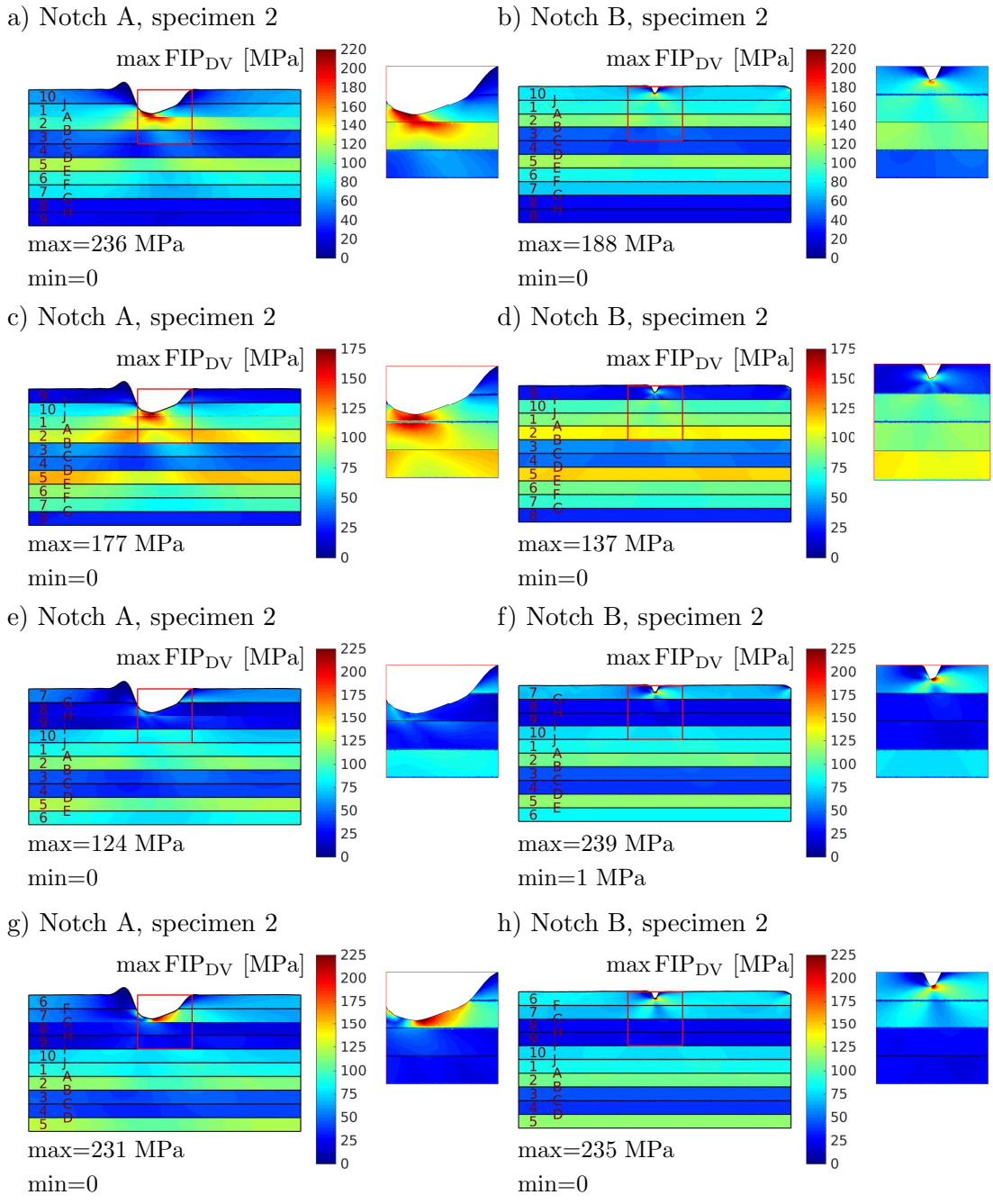

Figure 21: Distribution of FIP_{DV} in specimen 2 depending on the ordering of the grains. The results are obtained in the last load cycle.

holds values that are equal to or greater than those at notch B. This is an indication of the $\mathrm{FIP_{FS}}$ results observed in Fig.16. Since this parameter is a reflection of the slip activity, notch A correspondingly holds higher values than notch B. Apparently the modified Fatemi-Socie parameter $\mathrm{FIP_{FS}}$ provides an interpretation of the fatigue crack initiation conditions which to some extent is conflicting with the results based on FIP_ε and FIP_E. Using $\mathrm{FIP_{DV}}$, the results obtained are in relatively good agreement - although not perfectly - with the results based on $\mathrm{FIP_{FS}}$. A tentative conclusion is that either $\mathrm{FIP_{FS}}$ - reflecting local slip activity - or $\mathrm{FIP_{DV}}$ - reflecting the local slip system stress state - can be used as complementary indicators together with, for example, macroscopic stress concentrations and parameters such as FIP_ε and FIP_E, to give a more comprehensive view when localizing probable fatigue crack initiation sites. Noting the limited extent of plasticity in the present case, a purely stress-based criterion as $\mathrm{FIP_{DV}}$ might be of higher relevance than $\mathrm{FIP_{FS}}$, which depends on the amount of local plastic slip.

The influence of different grain stacking sequences is quite significant, as evident in Figs. 18 and 19. Naturally, the variations in the $\mathrm{FIP_{FS}}$ distribution is more evident in specimen 1, being exposed to a higher load amplitude than specimen 2. Noting that local slip activity and accumulation of slip (dislocations) at grain boundaries is often observed to coincide with the location of fatigue crack initiation, the effect of altering the grain sequence gives a plausible explanation for the more likely fatigue crack initiation at notch A than at notch B, as observed in the experiments in [1]. The same trends are shown also when considering $\mathrm{FIP_{DV}}$.

Combining the information gathered so far, it can be noted for both specimens 1 and 2 that:

1. The stress gradient beneath notch A is not as steep as at notch B.

2. The region of high axial stress is larger beneath notch A compared to notch B, although the stress magnitude is higher at notch B.

3. The region of non-zero effective plastic strain, as well as stored energy, extends further into the material beneath notch A compared to notch B, although the magnitudes are higher at notch B.

4. The magnitudes of the critical resolved shear stress is comparable at notch A and B, but indicate possible influence of grain orientation on the near-notch conditions.

5. The magnitude of the maximum plastic slip is higher - *and* the spatial extent of the slip activity is greater - at notch A compared to notch B.

Taken together, these observations indicate that - although the macroscopic stress concentration is higher at notch B - the less steep stress gradients and more widespread plastic slip activity may be the causes for notch A being the actual site for fatigue crack initiation. These observations, which involve not only the stress concentration but also the stress gradient, are in agreement with the classical studies on gradient effects at stress concentrations by Neuber

[38] and Sibel and Stieler [44]. In such analyses it is the stress conditions in a material *region*, rather than at a single point, that govern fatigue crack initiation.

Further, looking at the distributions of the $\mathrm{FIP}_{\mathrm{FS}}$ and $\mathrm{FIP}_{\mathrm{DV}}$ parameters and investigating different grain ordering sequences in Figs. 16-21, notch A is more prone to fatigue crack initiation than notch B for some grain sequences and the opposite holds for other configurations. Still, the results show that the local crystallographic texture may cause some notches to be more prone to fatigue crack initiation than others, regardless of the macroscopic stress concentration at the same location.

The slip activity in the grain structure is controlled by the availability of slip systems which can accommodate any crystallographic incompatibilities across grain boundaries. If two neighboring grains have different Schmid factors, the one with the highest Schmid factor will have the lowest yield stress and start to deform first. Stress concentrations will form in the stronger grain along the grain boundary and cause accumulation of geometrically necessary dislocations in order to accommodate strain compatibility between the grains. Such slip concentrations are seen in the present simulations, for example in Fig. 15. Regions with a high presence of geometrically necessary dislocations have been found to correlate faithfully with the locations of fatigue crack nucleation [46]. This motivates using a slip-dependent FIP such as the presently employed $\mathrm{FIP}_{\mathrm{FS}}$ to trace fatigue crack initiation sites. A related view of the stress state on individual slip systems is provided by $\mathrm{FIP}_{\mathrm{DV}}$, which provides results which are qualitatively quite similar to those obtained by using $\mathrm{FIP}_{\mathrm{FS}}$.

To further examine the likelihood for fatigue crack initiation to occur in the material's interior, rather than at the surface, experimental observations discussed in the literature can be considered. For example; in the experimental studies on Al6082 presented in [4], it is observed that microstructure variations may trigger fatigue crack initiation in the interior of the material rather than at the specimen surface. The crack path found in [4] is perpendicular to the loading direction as also seen in the present case, cf. Fig. 2, and it is noted in [4] that internal crack initiation sites may be "featureless", i.e. the initiation sites do not show any evidence of particle inclusions or other inhomogeneities. A similar observation is made in [22] where fatigue crack initiation in non-heat treated Al6082 occur most frequently at interior sites in the material where no particles or other features are present. Internal fatigue crack initiation sites, which do not show evidence of particle inclusions, are also observed in wrought Al6082-T5 in [42]. In the latter study, fatigue cracks are found to initiate at single grains with high Schmid factors and which are exposed to significant local plastic slip. The grains at which fatigue crack initiation occur are highly misoriented relative to the surrounding crystals. Fatigue experiments on extruded AA6082, performed in [37], show that fatigue crack initiation in this material typically involve intergranular separation.

The crystal plasticity simulations presented in [48] imply that the number of active slip systems is drastically reduced under cyclic plastic loading. After several cycles, single slip can be expected for small strain amplitudes. It is further discussed that this shift towards single slip is likely to be related to the formation of persistent shear bands (PSBs) which

may subsequently be instrumental in initiation of fatigue fracture, especially in the junction regions between PSBs and grain boundaries. A related discussion is given in [29], where slip is found to be increasingly confined within in bands which are aligned approximately 45° with respect to the loading direction, during cyclic plastic loading. The localized plastic slip is then assumed to be related to fatigue crack initiation by formulating a FIP which is fulfilled as the locally accumulated plastic slip equals a threshold value. This is seen to occur primarily at the intersections between significant local slip activity and grain boundaries. The same tendency towards slip activity, confined to bands with a 45° tilt relative to the loading direction and slip accumulation primarily at grain boundaries is seen also in the present simulations, for example in Figs. 15 and 18.

5 Concluding remarks

The motivation for the present work lies in the extensive experimental investigations of fatigue failures in extruded Al6082-T6, conducted in [1]. A somewhat unexpected outcome of the study was that the majority of fatigue failures were initiated at surface irregularities which did not correspond to the most significant macroscopic stress concentrations. Since the depths of the surface irregularities are comparable to microstructure features, such as the grain size, the present study aims at investigating if microstructure variations can be an explanation of the observed material behavior. The investigation is performed using crystal plasticity simulations and simulation models which are based on the actual surface geometries and material microstructures encountered in the experiments. The present simulations show that variations in the microstructure can indeed make initiation of fatigue more likely to occur at surface notches which have macroscopic stress concentrations lower than maximum. Different fatigue initiation parameters (FIP) which are frequently employed in the literature are investigated and it is shown that a FIP based on a modified Fatemi-Socie criterion, or alternatively a FIP based on the Dang Van criterion, adds valuable information on local slip system activity which is to some extent conflicting with results based on other FIPs, e.g. based on accumulated plastic strain or stored energy. A key observation is that macroscopic stress concentrations alone do not tell the full story - as is also vividly evident from the experiments in [1] - and that crystal plasticity simulations provide a competent additional tool in analyzing fatigue crack initiation mechanisms in polycrystalline samples.

The present investigation highlights the influence of microstructure heterogeneities on fatigue properties in polycrystals and topics which will be considered in follow-up work comprise, for example, further microstructure characterization of individual notches, e.g. by EBSD mapping. In addition, a combination of crystal plasticity simulations and experimental data will also be considered for fatigue life predictions. In these planned studies, the densities of different dislocation species as well as elastic anisotropy will also be considered in the crystal plasticity model.

References

[1] S.K. Ås. *Fatigue life predicition of an aluminium alloy automotive component using finite element analysis of surface topography.* PhD thesis, Norwegian University of Science and Technology, Department of Structural Engineering, 2006.

[2] S.K. Ås, B. Skallerud, and B.W. Tveiten. Surface roughness characterization for fatigue life predictions using finite element analysis. *Int. J. Fatigue*, 30:2200–2209, 2008.

[3] S.K. Ås, B. Skallerud, B.W. Tveiten, and B. Holme. Fatigue life prediction of machined components using finite element analysis of surface topography. *Int. J. Fatigue*, 27(10-12):1590–1596, 2005.

[4] J. Bach, H.W. Höppel, M. Prell, and M. Göken. Crack initiation mechanisms in AA6082 fatigued in the VHCF-regime. *Int. J. Fatigue*, 60:23–27, 2014.

[5] V.P. Bennett and D.L. McDowell. Polycrystal orientation distribution effects on microslip in high cycle fatigue. *Int. J. Fatigue*, 25:27–39, 2003.

[6] D. Bufford, Y. Liu, J. Wang, H. Wang, and X. Zhang. *In situ* nanoindentation study on plasticity and work hardening in aluminium with incoherent twin boundaries. *Nature Communications*, 5:4864, 2014.

[7] E.P. Busso and G. Cailletaud. On the selection of active slip systems in crystal plasticity. *Int. J. Plasticity*, 21:2212–2231, 2005.

[8] G.M. Castelluccio and D.L. McDowell. A mesoscale approach for growth of 3D microstructurally small fatigue cracks in polycrystals. *Int. J. Damage Mech.*, 23(6):791–818, 2014.

[9] K.-S. Cheong and E.P. Busso. Effects of lattice misorientations on strain heterogeneities in FCC polycrystals. *J. Mech. Phys. Solids*, 54:671–689, 2006.

[10] B. Crossland. Effect of large hydrostatic pressures on the torsional fatigue strength of an alloy steel. In *Proceedings of the international conference on fatigue of metals*, pages 138–149, London, 1956.

[11] V.K. Dang. *Sur la résistance à la fatigue des métaux.* PhD thesis, Université de Paris VI, 1971.

[12] V.S. Deshpande, A. Needleman, and E. Van der Giessen. Discrete dislocation modeling of fatigue crack propagation. *Acta Mater.*, 50(4):831–846, 2002.

[13] L.P. Evers, W.A.M. Brekelmans, and M.G.D. Geers. Non-local crystal plasticity model with intrinsic SSD and GND effects. *J. Mech. Phys. Solids*, 52:2379–2401, 2004.

[14] L.P. Evers, W.A.M. Brekelmans, and M.G.D. Geers. Scale dependent crystal plasticity framework with dislocation density and grain boundary effects. *Int. J. Solids Struct.*, 41:5209–5230, 2004.

[15] L.P. Evers, D.M. Parks, W.A.M. Brekelmans, and M.G.D. Geers. Crystal plasticity model with enhanced hardening by geometrically necessary dislocation accumulation. *J. Mech. Phys. Solids*, 50:2403–2424, 2002.

[16] F. Farukh, L.G. Zhao, R. Jiang, P. Reed, D. Proprentner, and B.A. Shollock. Realistic microstructure-based modelling of cyclic deformation and crack growth using crystal plasticity. *Comput. Mater. Sci.*, 11:395–405, 2016.

[17] A. Fatemi and D.F. Socie. A critical plane approach to multiaxial fatigue damage including out-of-phase loading. *Fatigue Fract. Eng. M.*, 11(3):149–165, 1988.

[18] K. Gillner and S. Münstermann. Numerically predicted high cycle fatigue properties through representative volume elements of the microstructure. *Int. J. Fatigue*, 105:219–234, 2017.

[19] S. Groh, E.B. Marin, M.F. Horstemeyer, and H.M. Zbib. Multiscale modeling of the plasticity in an aluminum single crystal. *Int. J. Plasticity*, 25:1456–1473, 2009.

[20] S. Güngör and L. Edwards. Effect of surface texture on the initiation and propagation of small fatigue cracks in a forged 6082 aluminium alloy. *Mater. Sci. Eng. A*, 160:17–24, 1993.

[21] P. Håkansson, M. Wallin, and M. Ristinmaa. Prediction of stored energy in polycrystalline materials during cyclic loading. *Int. J. Solids Struct.*, 45:1570–1586, 2008.

[22] H.W. Höppel, L. May, M. Prell, and M. Göken. Influence of grain size and precipitation state on the fatigue lives and deformation mechanisms of CP aluminium and AA6082 in the VHCF-regime. *Int. J. Fatigue*, 33:10–18, 2011.

[23] D. Jíša, Liškutín, T. Kruml, and J. Polák. Small fatigue crack growth in aluminium alloy EN-A

6082/T6. *Int. J. Fatigue*, 32:1913–1920, 2010.
[24] R.C. Juvinall. *Engineering Considerations of Stress, Strain, and Strength*. McGraw-Hill, 1967.
[25] S.R. Kalidindi, A. Bhattacharyya, and R.D. Doherty. Detailed analyses of grain-scale plastic deformation in columnar polycrystalline aluminium using orientation image mapping and crystal plasticity models. *Proc. R. Soc., London*, 460:1935–1956, 2004.
[26] A.M. Korsunsky, D. Dini, F.P.E. Dunne, and M.J. Walsh. Comparative assessment of dissipated energy and other fatigue criteria. *Int. J. Fatigue*, 29:1990–1995, 2007.
[27] R.W. Landgraf, J. Morrow, and T. Endo. Determination of the cyclic stress-strain curve. *J. Mater.*, 4(1):176–188, 1969.
[28] L. Li, L. Shen, and G. Proust. Fatigue crack initiation life prediction for aluminium alloy 7075 using crystal plasticity finite element simulations. *Mech. Mater.*, 81:84–93, 2015.
[29] A. Manonukul and F.P.E. Dunne. High- and low-cycle fatigue crack initiation using polycrystal plasticity. *Proc. R. Soc., London A*, 460:1881–1903, 2004.
[30] T. Matake. An explanation on fatigue limit under combined stress. *Bull. JSME*, 20:257–263, 1977.
[31] D.L. McDowell. Simulation-based strategies for microstructure-sensitive fatigue modeling. *Mater. Sci. Eng. A*, 468-470:4–14, 2007.
[32] D.L. McDowell and F.P.E. Dunne. Microstructure-sensitive computational modeling of fatigue crack formation. *Int. J. Fatigue*, 32:1521–1542, 2010.
[33] D.L. Medlin, C.B. Carter, J.E. Angelo, and M.J. Mills. Climb and glide of $a/3\langle 111\rangle$ dislocations in an aluminium $\Sigma = 3$ boundary. *Phil. Mag. A*, 75(3):733–747, 1997.
[34] L. Méric, G. Cailletaud, and M. Gaspérini. F.E. calculations of copper bicrystal specimens submitted to tension-compression. *Acta Metall. Mater.*, 42(3):921–935, 1994.
[35] G. Mrówka-Nowotnik and J. Sieniawski. Influence of heat treatment on the microstructure and mechanical properties of 6005 and 6082 aluminium alloys. *J. Mater. Process. Technol.*, 162-163:367–372, 2005.
[36] W.D. Musinski and D.L. McDowell. Simulating the effect of grain boundaries on microstructurally small fatigue crack growth from a focused ion beam notch through a threedimensional array of grains. *Acta Mater.*, 112:20–39, 2016.
[37] N.E. Nanninga. *High cycle fatigue of AA6082 and AA6063 aluminum extrusions*. PhD thesis, Michigan Technological University, 2008.
[38] H. Neuber. *Theory of Notch Stresses*. Springer-Verlag, second edition, 1958.
[39] J. Rossiter, A. Brahme, M.H. Simha, K. Inal, and R. Mishra. A new crystal plasticity scheme for explicit time integration codes to simulate deformation in 3D microstructures: Effects of strain path, strain rate and thermal softening on localized deformation in the aluminum alloy 5754 during simple shear. *Int. J. Plasticity*, 26:1702–1725, 2010.
[40] M.D. Sangid. The physics of fatigue crack intiation. *Int. J. Fatigue*, 57:58–72, 2013.
[41] E. Schmid and W. Boas. *Plasticity of crystals with special reference to metals*. F.A. Hughes & Co. Ltd, 1950.
[42] D. Schwerdt, B. Pyttel, C. Berger, M. Oechsner, and U. Kunz. Microstructure investigations on two different aluminum wrought alloys after very high cycle fatigue. *Int. J. Fatigue*, 60:28–33, 2014.
[43] M. Shenoy, J. Zhang, and D.L. McDowell. Estimating fatigue sensitivity to polycrystalline Ni-base superalloy micostructures using a computational approach. *Fatigue Fract. Eng. M.*, 30:889–04, 2007.
[44] E. Siebel and M. Stieler. Ungleichförmige Spannungsverteilung bei schwingender Beanspruchung. *Z. Ver Deutsch. Ing.*, 97:121–126, 1955.
[45] N. Sukumar, D.L. Chopp, and B. Moran. Extended finite element method and fast marching method for three-dimensional fatigue crack propagation. *Eng. Fract. Mech.*, 70(1):29–48, 2003.
[46] C.A. Sweeney, W. Vorster, S.B. Leen, E. Sakurada, P.E. McHugh, and F.P.E. Dunne. The role of elastic anisotropy, length scale and crystallographic slip in fatigue crack nucleation. *J. Mech. Phys. Solids*, 61:1224–1240, 2013.
[47] D. Taylor. *The Theory of Critical Distances: A New Perspective in Fracture Mechanics*. Elsevier

Science Ltd., Oxford, UK, 2007.
[48] L.S. Tóth, A. Molinari, and N. Zouhal. Cyclic plasticity phenomena as predicted by polycrystal plasticity. *Mech. Mater.*, 32:99–113, 2000.
[49] K.D. Van, B. Griveau, and O. Massage. On a new multiaxial fatigue limit criterion: Theory and applications. In M.W. Brown and K.J. Miller, editors, *Biaxial and Multiaxial Fatigue, EGF 3*, pages 479–496. Mechanical Engineering Publications, London, 1989.
[50] V.V.C. Wan, D.W. MacLachlan, and F.P.E. Dunne. A stored energy criterion for fatigue crack nucleation in polycrystals. *Int. J. Fatigue*, 68:90–102, 2014.
[51] K.-S. Zhang, J.W. Ju, Z. Li, Y.-L. Bai, and W. Brocks. Micromechanics based fatigue life prediction of a polycrystalline metal applying crystal plasticity. *Mech. Mater.*, 85:16–37, 2015.